DNA Devices in Serum and the Cell

Hieu Bui and John Reif
Duke University

The success of DNA nanotechnology comes from three key ingredients:

1) Our quantitative understanding of DNA thermodynamics, which makes it possible to predict reliably how single-stranded DNA molecules fold and interact with one another
2) The rapid falling cost and increasing quality of DNA synthesis
3) The focus on cell-free settings, where designed reaction pathways can proceed without interference from DNA and RNA processing enzymes and other confounding factors that might be encountered in cells

Y. J. Chen, B. Groves, R. A. Muscat, G. Seelig, DNA nanotechnology from the test tube to the cell. *Nature nanotechnology* 10, 748-760 (2015).

DNA Nanotechnology from the Test tube to the Cell

Talk describes recent progress towards the goal of bringing DNA nanotechnology into the cell

Focus:

Nucleic acid nanodevices and nanostructures that are rationally designed, chemically synthesized and then delivered to mammalian cells.

Y. J. Chen, B. Groves, R. A. Muscat, G. Seelig, DNA nanotechnology from the test tube to the cell. *Nature nanotechnology* 10, 748-760 (2015).

Application of DNA nanotechnology at the interface with biology

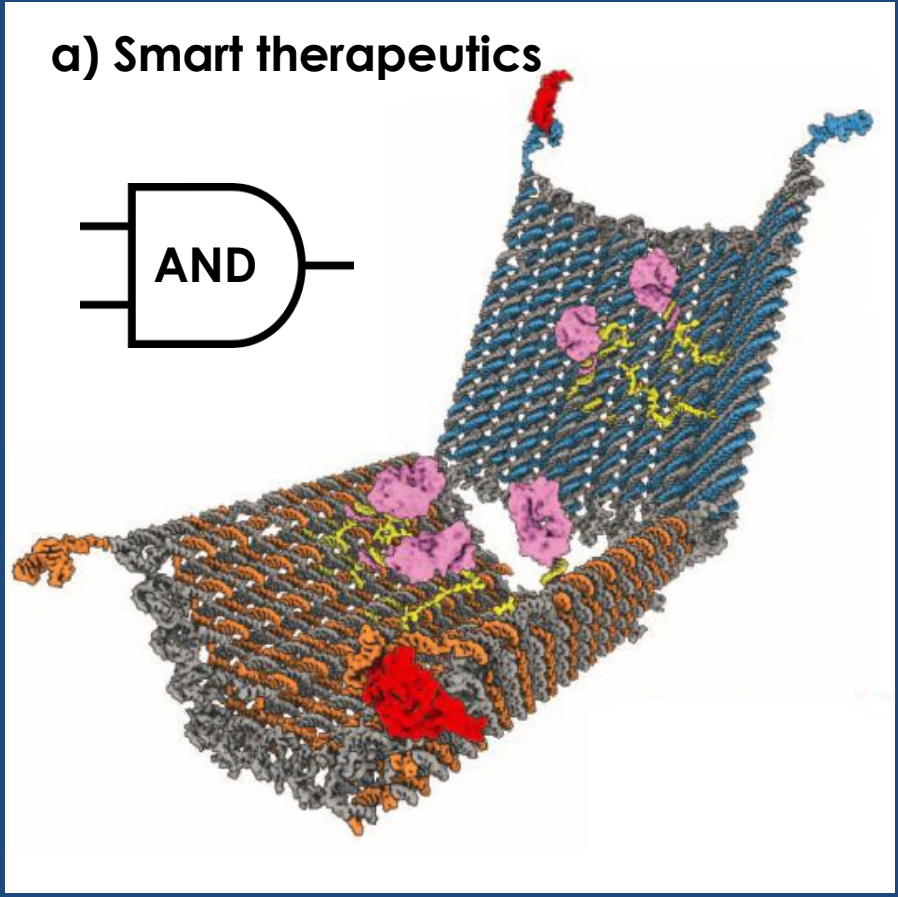

Smart therapeutics could combine structural elements with molecular logic to target therapeutic actions to a specific cell or tissue type, thus minimizing side effects.

Douglas, S. M., Bachelet, I. & Church, G. M. A logic-gated nanorobot for targeted transport of molecular payloads. Science 335, 831–834 (2012)

Application of DNA nanotechnology at the interface with biology

b) Drug delivery

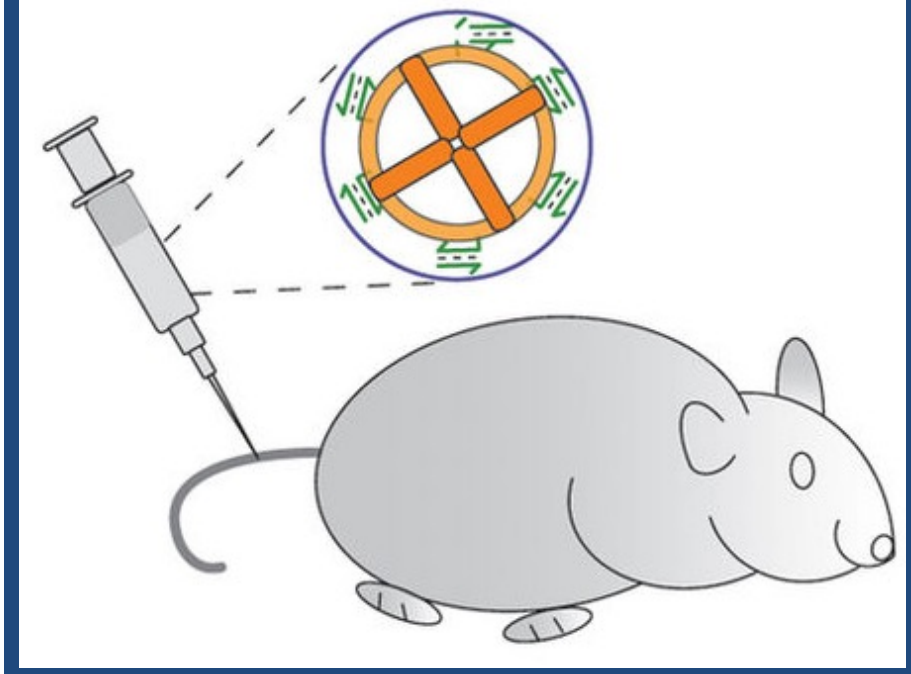

DNA nanostructures can serve as programmable scaffolds for attaching drugs, targeting ligands and other modifications, such as lipid bilayers.

Perrault, S. D. & Shih, W. M. Virus-inspired membrane encapsulation of DNA nanostructures to achieve in vivo stability. ACS Nano 8, 5132–5140 (2014)

Application of DNA nanotechnology at the interface with biology

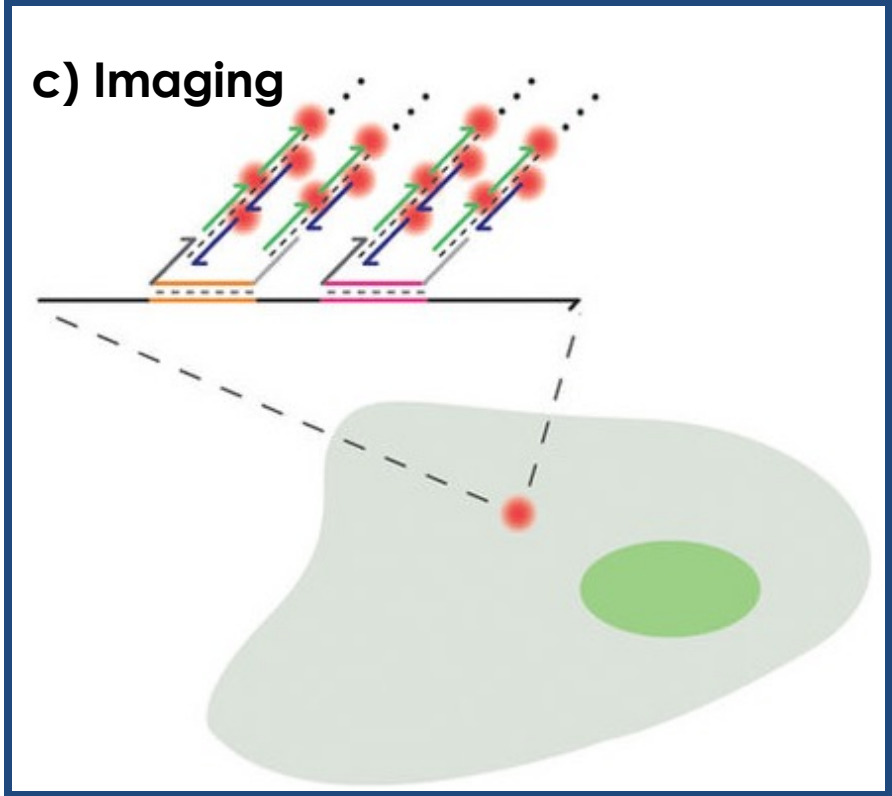

A novel class of sensitive and specific imaging probes that takes advantage of DNA-based amplification mechanisms can be programmed to sequence-specifically interact with cellular RNA.

Choi, H. M. T., Beck, V. A. & Pierce, N.
A. Next-generation in situ hybridization chain reaction: higher gain, lower cost, greater durability. ACS Nano 8, 4284–4294 (2014)

Application of DNA nanotechnology at the interface with biology

d) Cell biology

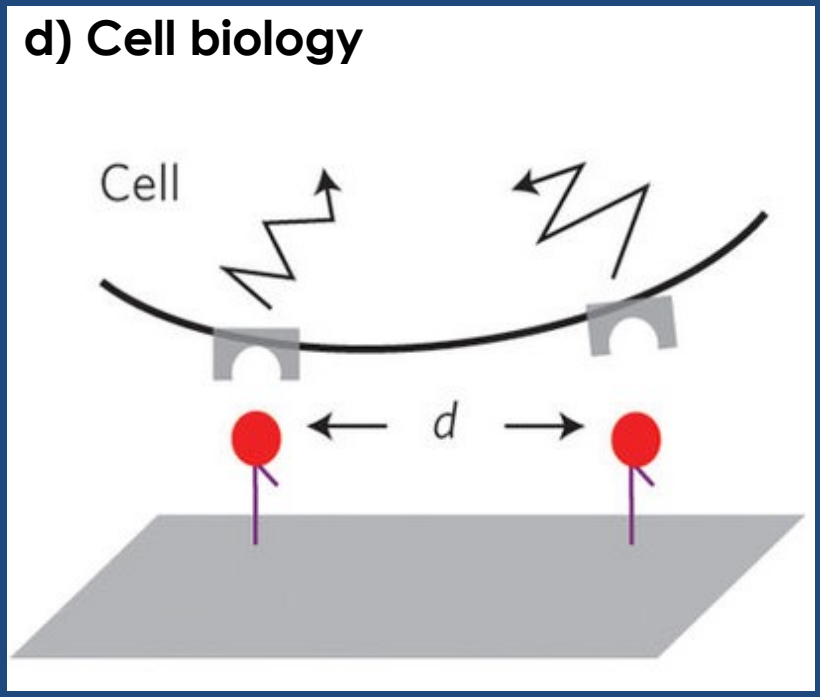

DNA origami and other structures provide precise control over the spatial organization of functional molecular groups, which makes them intriguing tools for quantitative measurements in cell biology.

Shaw, A. et al. Spatial control of membrane receptor function using ligand nanocalipers. Nature Methods 11, 841–846 (2014)

Cell Surface Computation

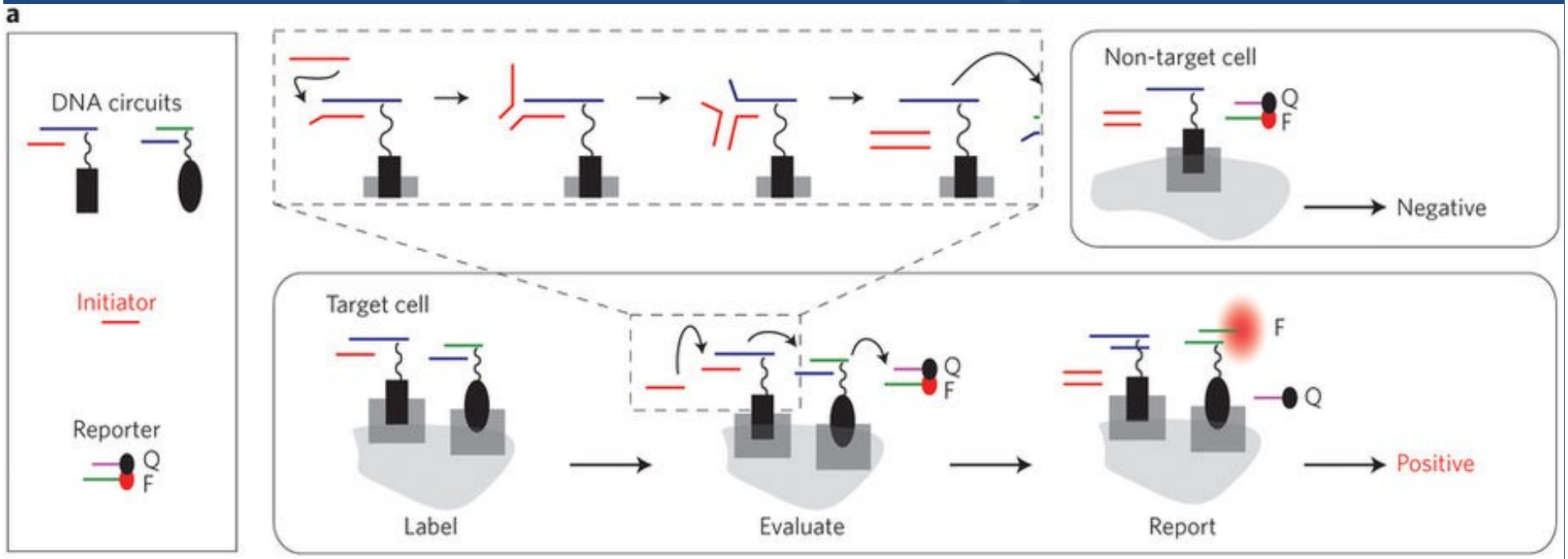

***In situ* cell classification by evaluating specific surface markers:**

[Rudchenko, M. et al. Autonomous molecular cascades for evaluation of cell surfaces. Nature Nanotech. 8, 580–586 (2013).]

- Cells are first coated with DNA-modified antibodies (DNA circuits; antibodies are shown as rectangles or ellipses, DNA strands as colored lines), and depending on the surface marker profiles of the cell type, either one or two gates can bind to cells.

- **The subsequent introduction of an initiator strand (red) triggers a series of strand displacement reactions (fully complementary strands share the same colors).**
- **A soluble reporter complex can fluorescently tag only cells labeled with two surface-bound gates**

Cell Surface Computation

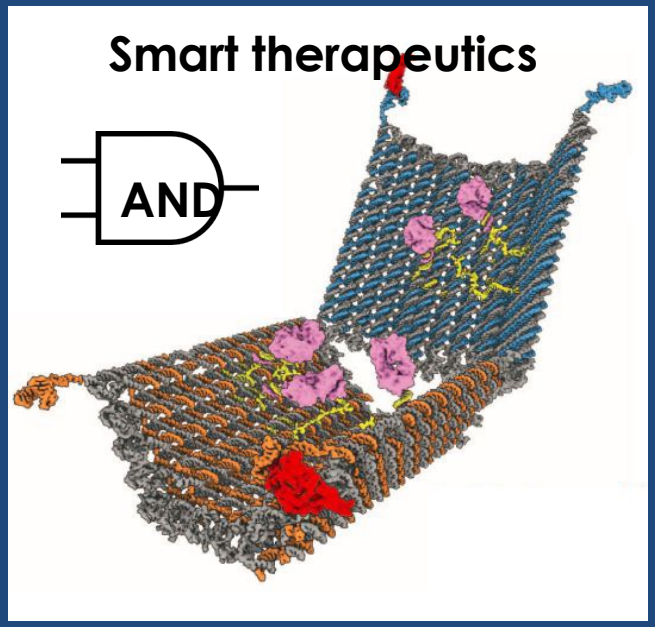

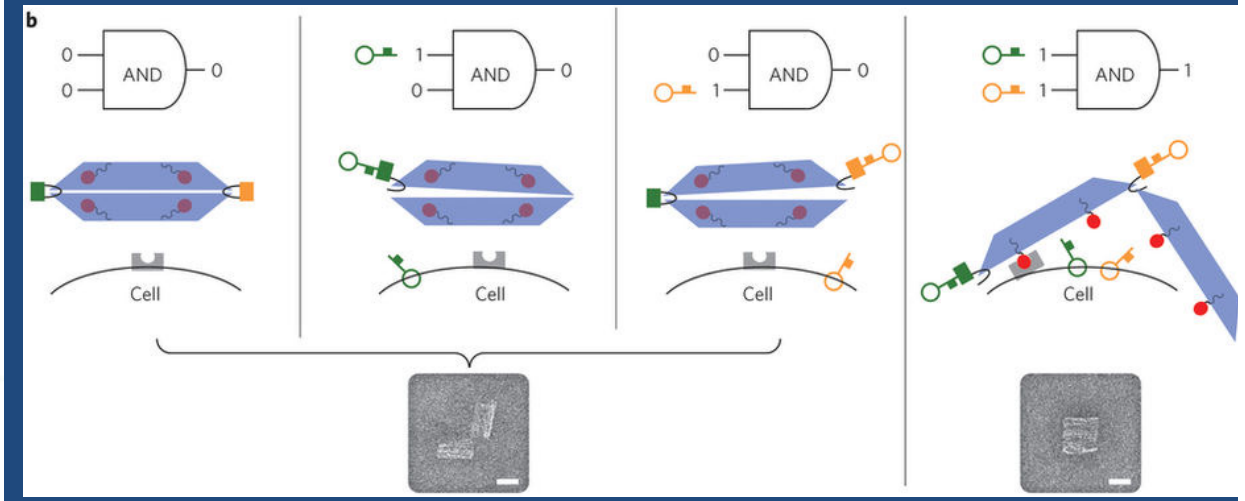

Molecular robot for targeting a therapeutic action to specific cell types:

The schematic shows how a barrel-shaped nanorobot responds to specific antigens (keys) expressed on cells surfaces.

(Douglas, S. M., Bachelet, I. & Church, G. M. A logic-gated nanorobot for targeted transport of molecular payloads. Science 335, 831–834 (2012).)

The nanorobot is initially held in a closed configuration by two aptamer locks; only when it encounters a cell that displays two matching antigens can it be opened, thereby exposing a drug.

Bottom: Transmission electron microscopy images of the closed and open states of the nanorobots (scale bars, 20 nm).

Programming DNA-Based Biomolecular Reaction Networks on Cancer Cell Membranes

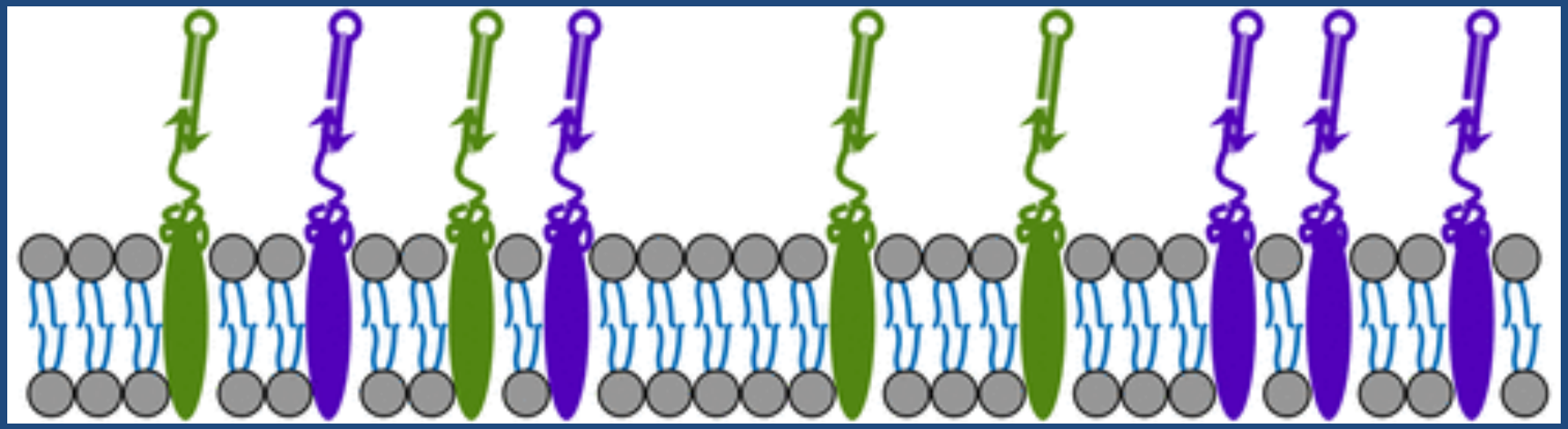

Tianqi Song, Shalin Shah, Hieu Bui, Sudhanshu Garg, Abeer Eshra, Ming Yang, and John Reif, Programming DNA-Based Biomolecular Reaction Networks on Cancer Cell Membranes, Journal of the American Chemical Society (JACS), Vol. 141, No. 42, pp. 16539-16543. (Oct 2019). https://doi.org/10.1021/jacs.9b05598

Programming DNA-Based Biomolecular Reaction Networks on Cancer Cell Membranes

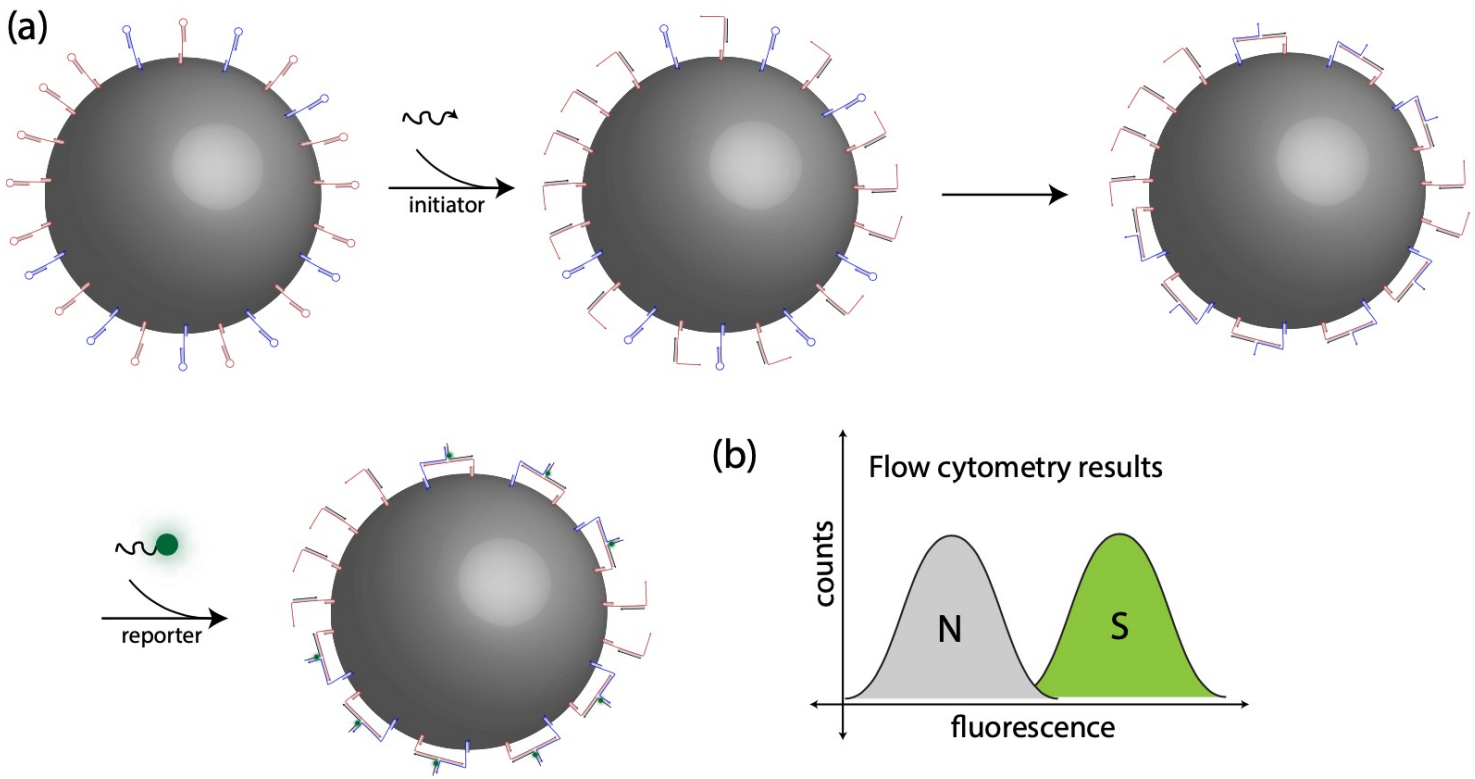

A high-level description of our architecture:

(a) An example reaction network by our architecture. This is a 2-layer linear cascade reaction network, and there are two types of nodes in the network that are indicated by two different colors, where each node is a DNA hairpin connected with a DNA aptamer, where a DNA aptamer is a DNA strand that can be rationally designed and recognize a particular cell membrane receptor which can range from small molecules to proteins using a DNA aptamer via aptamer-receptor binding.

- When operating the reaction network, we first mix the nodes with the cancer cells in a reaction buffer. If both targeted receptors exist on the membrane, both nodes will be localized on the membrane by aptamer-receptor binding. We then filter out the free nodes in the buffer to exclude potential non-localized reactions.
- By introducing the initiator strands, the 2-layer linear cascade reaction is started. First, the initiator opens up the red hairpin by DNA strand displacement.
- Then, the output strand from the red hairpin opens up the blue hairpin. The output strand from the blue hairpin can hybridize with a reporter DNA strand (conjugated with a fluorophore), such that the cancer cells are labeled by the fluorophore and can be recognized by flow cytometry.

(b) Group "S": cancer cells labeled by fluorophore via a reaction network on the membrane: Group "N": cancer cells of the same type without fluorophore. Note that the density of each node on the cell membrane is determined by the density of the corresponding receptor, and the nodes can move on the cell membrane because of the mobility of the receptors.

Programming DNA-Based Biomolecular Reaction Networks on Cancer Cell Membranes

Node design and an example of 2-layer linear cascade:

(a) Node design:

- A node has two modules: a reaction module (black) and an addressing module (red).
- The two modules are connected by the DNA hybridization between A2 and A2∗, where A2∗ is the reverse complement of A2.
- The addressing module has an aptamer for targeting a particular cell membrane receptor.
- The initiator reacts with the reaction module (a DNA hairpin) to produce an output.
- The output has the same domain motif as the initiator, which makes it possible to cascade such nodes into reaction networks.

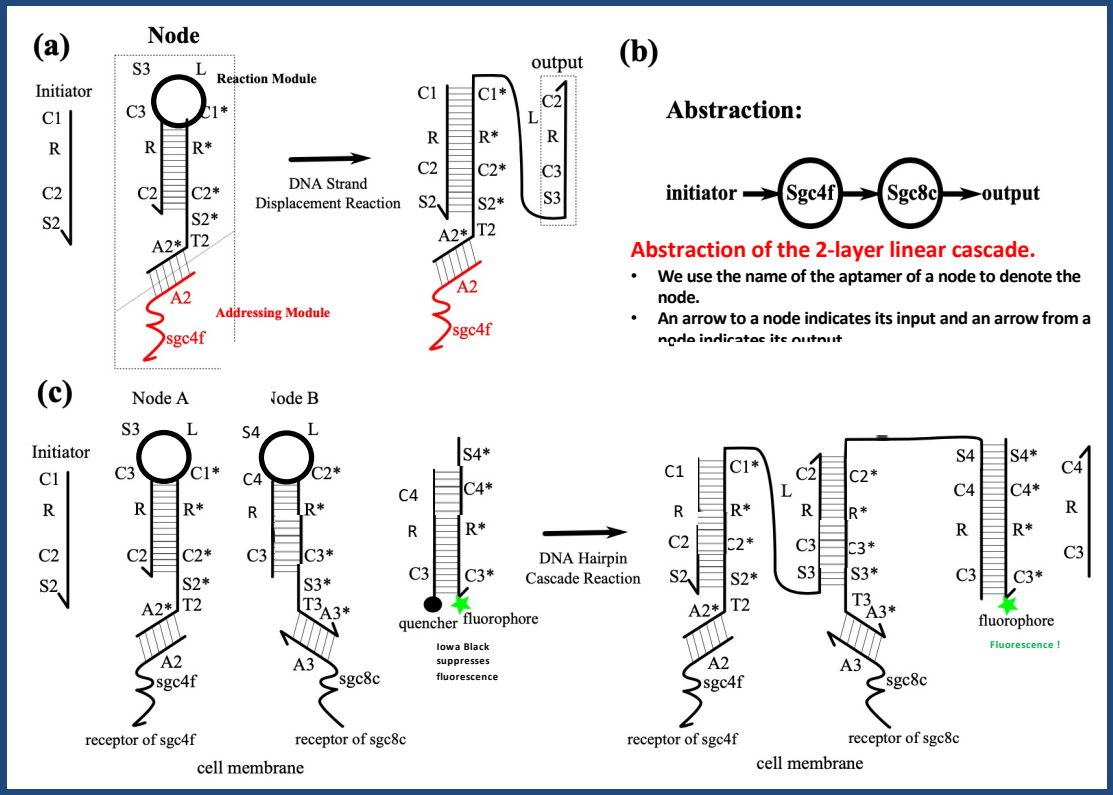

(c) An example reaction network which is a 2-layer linear cascade.

- The initiator starts the cascade reaction between node A and node B.
- The output of node B reacts with the reporter complex to tag the cell by a fluorophore.
- Note that reaction networks that are more complex than linear cascades can be built using the same logic.

Tianqi Song, Shalin Shah, Hieu Bui, Sudhanshu Garg, Abeer Eshra, Ming Yang, and John Reif, Programming DNA-Based Biomolecular Reaction Networks on Cancer Cell Membranes, Journal of the American Chemical Society (JACS), Vol. 141, No. 42, pp. 16539-16543. (Oct 2019). https://doi.org/10.1021/jacs.9b05598

Programming DNA-Based Biomolecular Reaction Networks on Cancer Cell Membranes

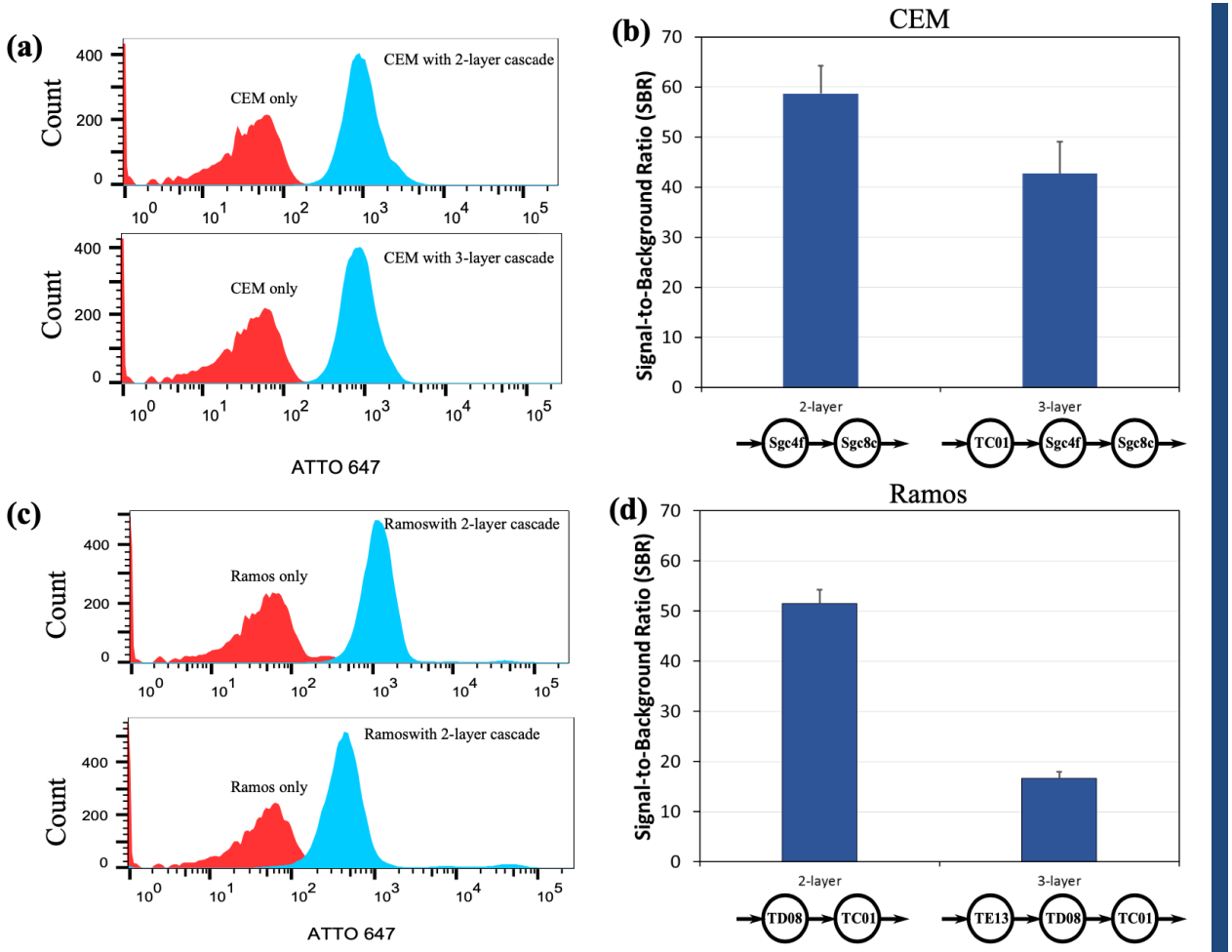

Linear cascades on cancer cell lines CCRF-CEM and Ramos.

(a) Flow cytometry result of a single repeat for testing 2-layer (top) and 3-layer (bottom) cascades on CCRF-CEM. Using the 2-layer cascade to explain, the cell population treated by the cascade has much stronger fluorescence intensity than the cell population without any treatment. We get the geometric means of fluorescence intensity for both populations, and calculate the ratio between the two geometric means (blue population over red population) to get a signal-to-background ratio (SBR). We repeat such an experiment for three times to get three SBRs and get the statistics in (b) (left), and it is the same for all reaction networks demonstrated in this paper. Note that the horizontal axis is fluorescence intensity (log-scale) and the vertical axis is cell count.

(b)Statistics of SBRs for linear cascades on CCRF-CEM from three repeats for each case. The abstractions at the bottom indicate the targets of each cascade.

(c) Flow cytometry result of a single repeat for testing 2-layer (top) and 3-layer (bottom) cascades on Ramos.

(d) Statistics of SBRs for linear cascades on Ramos from three repeats of each case.

DNA Nanomachines and Gates inside Cells

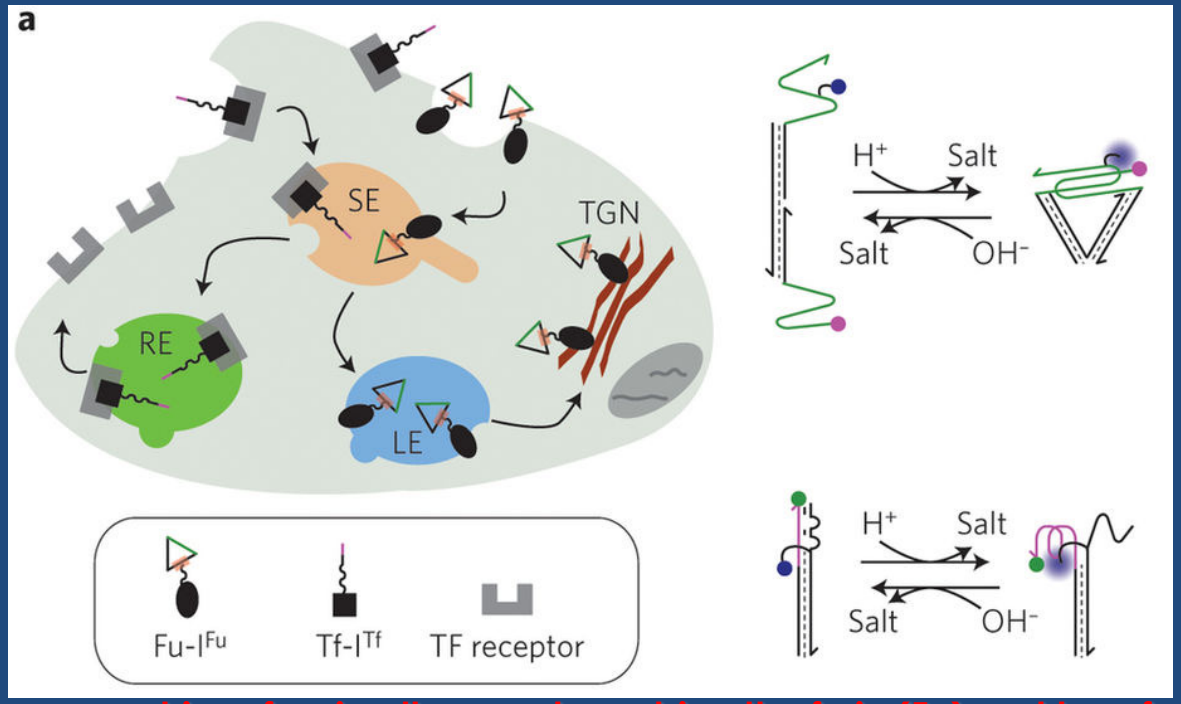

pH-sensitive DNA nanomachines for simultaneously probing the furin (Fu) and transferrin (Tf) pathways: (Modi, S., Nizak, C., Surana, S., Halder, S. & Krishnan, Y. Two DNA nanomachines map pH changes along intersecting endocytic pathways inside the same cell. Nature Nanotech. 8, 459–467 (2013).)

Left: A transferrin-modified DNA nanomachine Tf–ITf is confined to the transferrin pathway. The nanomachine enters a sorting endosome (SE), then a recycling endosome (RE), and eventually returns to the membrane.

The DNA nanomachine Fu–IFu targets the furin pathway: it enters the SE, then late endosome (LE), and eventually localizes in the trans-Golgi network (TGN). Nanomachine fluorescence is sensitive to pH, which varies between different endosomal compartments.

Right: pH-sensitive elements of DNA nanomachines: IFu (green strands, top) and DNA nanomachines Itf (pink strands, bottom) form i-motif at low pH, which causes high FRET between the two fluorophores

DNA Nanomachines and Gates inside Cells

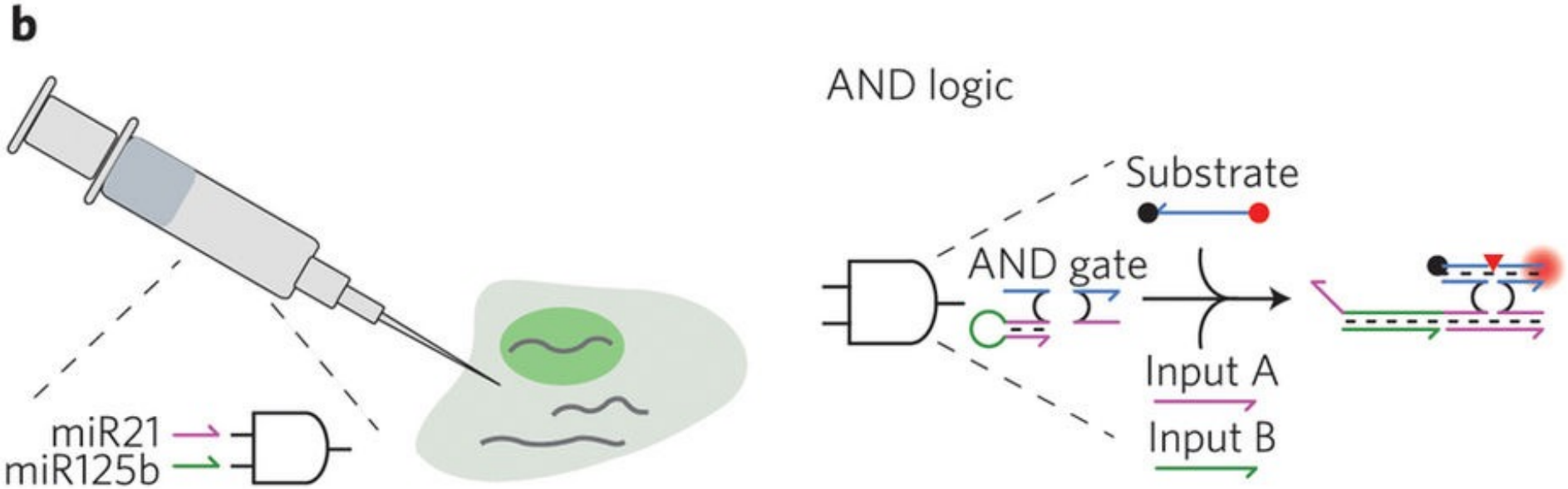

pH-sensitive DNA nanomachines for simultaneously probing the furin (Fu) and transferrin (Tf) pathways:
(Modi, S., Nizak, C., Surana, S., Halder, S. & Krishnan, Y. Two DNA nanomachines map pH changes along intersecting endocytic pathways inside the same cell. Nature Nanotech. 8, 459–467 (2013).)

A DNAzyme-based AND logic gate operates inside living cells:
Left: Synthesized inputs with the sequences of miR-21 and mir-125b are micro-injected together with the logic AND gate.
Right: Reaction mechanism. Input B first binds to the hairpin (green segment), which is then available to interact with input A to join the two components of the AND gate.
The joined DNAzyme complex can then cleave the substrate, thus leading to high fluorescence by separating a fluorophore (red dot) from a quencher (black dot).

Complexity Break for Cellular DNA Nanodevices

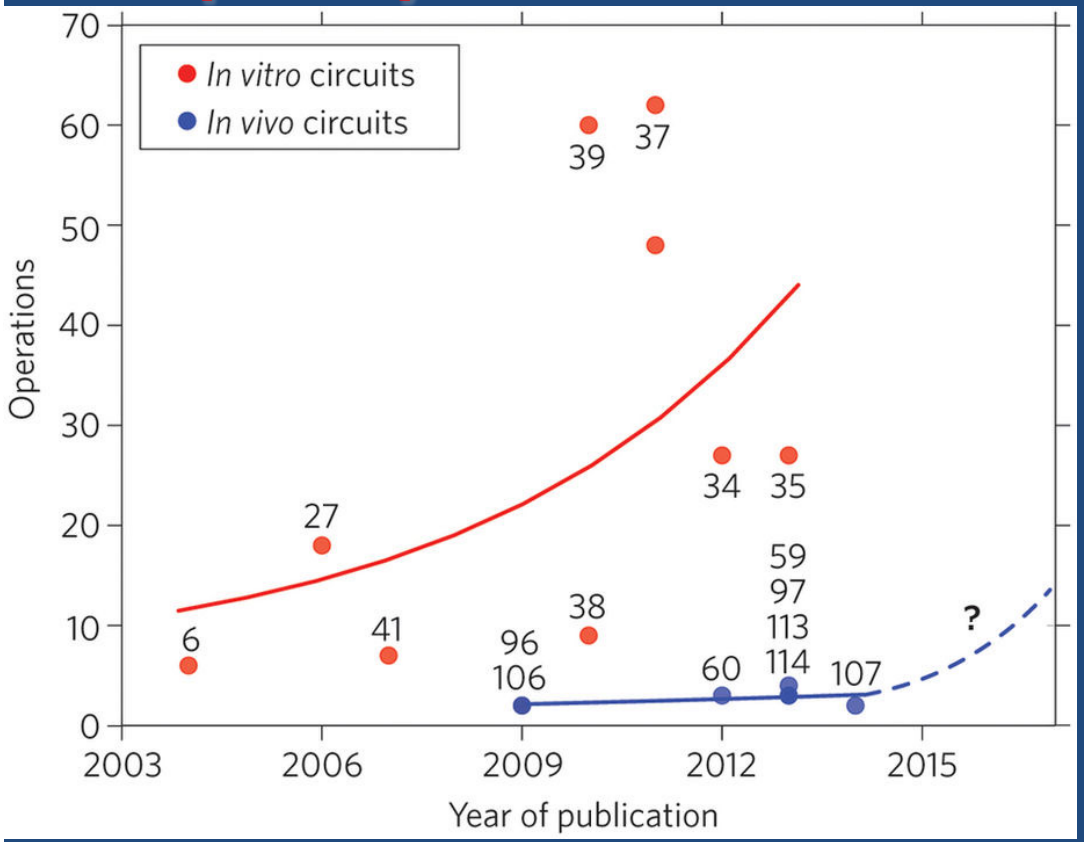

The complexity of cell-free DNA logic circuits and similar dynamic devices has increased by almost two orders of magnitude over the past decade.

In cellular settings, dynamic devices with only two or three independent operations have so far been demonstrated. This suggests that design principles for adapting dynamic DNA nanodevices to cells are yet to be uncovered.

- **Each colored dot and number represent a specific reaction network and associated publication (reference number); trend lines are included to guide the eye.**
- **An operation is defined as a unique (sequence-specific) connection, such as a strand displacement reaction or DNAzyme cleavage event within a network.**
- **A circuit with n gates arranged in a cascade is considered to be equally complex as a circuit with n independent gates operating in parallel, even though the latter is probably easier to realize experimentally.**
- **Moreover, multi-turnover catalytic reactions are weighed equally against single-step reactions, which potentially underestimates the complexity of the former**

Cellular half-lives of short, unmodified nucleic acids: minutes

Cell Lysates: mixtures of cellular components created from cells that have been homogenized, lacking a cell wall

Yan, et al test 12 hours DNA in cell lysates:

- Stable of DNA origami
- Long single- and double-stranded nucleic acids could not be recovered

Molecular crowding: The diffusion coefficient of synthetic DNA molecules in the cytoplasm is 5-100 times smaller than in water, depending on the size of the molecule.

DNA Topology Influences Molecular Machine Lifetime in Human Serum

Sara Goltry, Natalya Hallstrom, Tyler Clark, Wan Kuang, Jeunghoon Lee, Cheryl Jorcyk, William B. Knowlton, Bernard Yurke, William L. Hughes and Elton Graugnard, DNA topology influences molecular machine lifetime in human serum, Nanoscale, 2015, 7, 10382

A nanomachine and linear probe schematics:

(a) Three-state DNA nanomachine transitions between Relaxed, Closed, and Open states with the addition of fuel strands, ***F*₁** and ***F*₂** and their corn-plements, c***F*₁** and c***F*₂**. In the Relaxed state, the distance between the aye and quencher conjugated to double-stranded DNA segments Aland A2 is estimated to be —5 nm.
(b) The two-state linear probe transitions between the Bright and Dark states upon hybridization of the dye- labeled probe strand, P, and the quencher-labeled strand, a Strand dis-placement by ca releases P and restores fluorescence emission. The mechanical states are monitored by measuring the fluorescence emission from the devices.

Sara Goltry, Natalya Hallstrom, Tyler Clark, Wan Kuang, Jeunghoon Lee, Cheryl Jorcyk, William B. Knowlton, Bernard Yurke, William L. Hughes and Elton Graugnard, DNA topology influences molecular machine lifetime in human serum, Nanoscale, 2015, 7, 10382

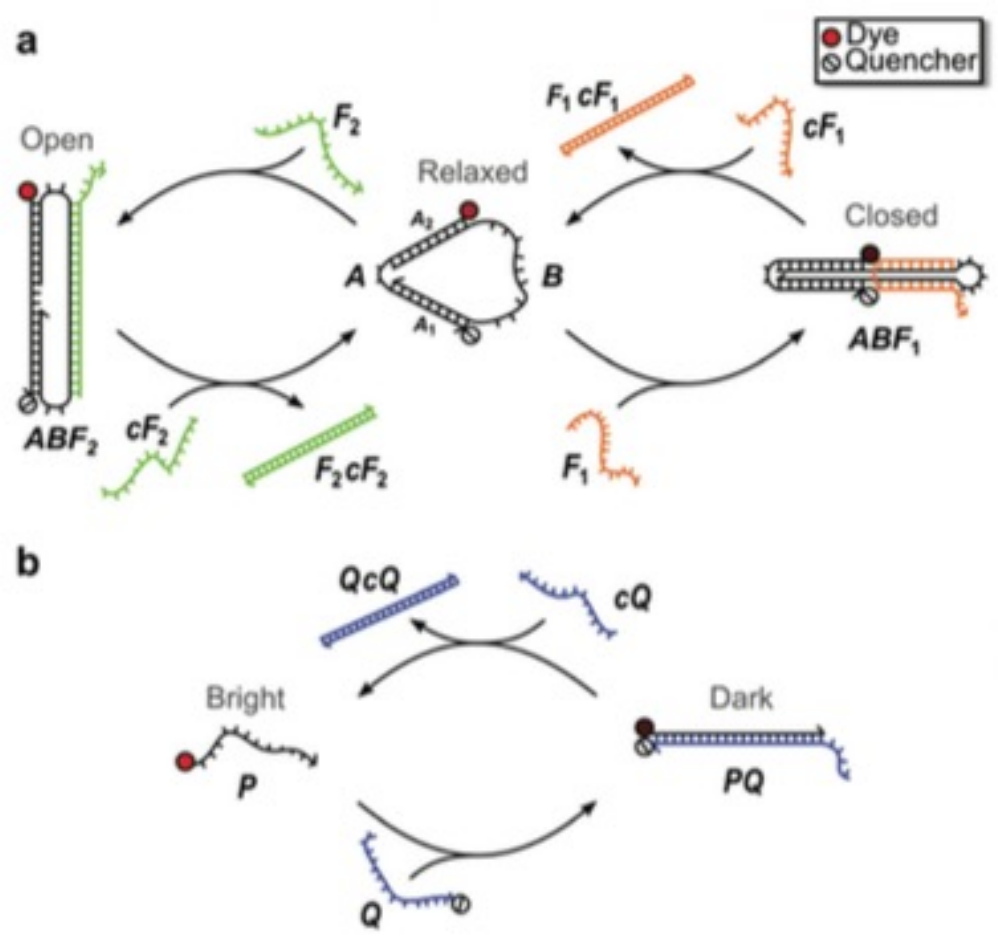

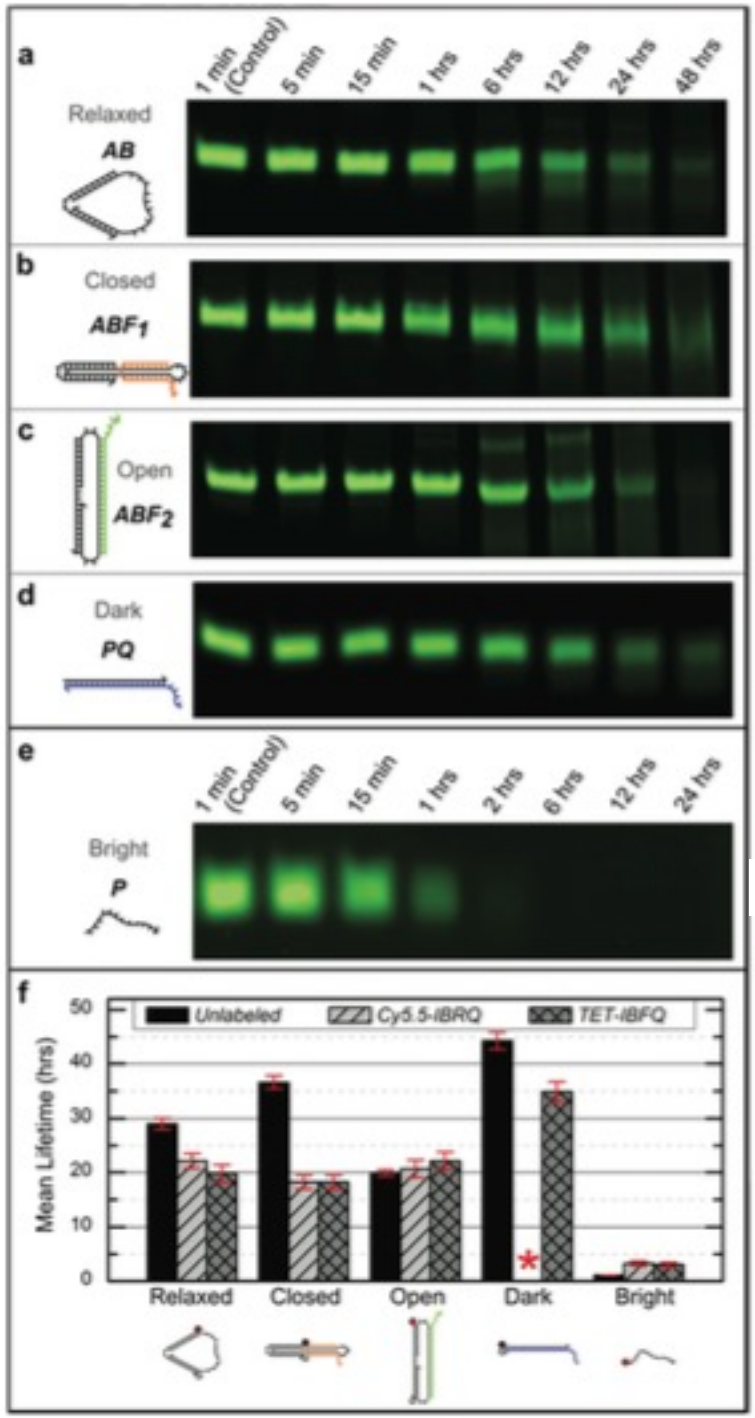

DNA Devices in 70% Human Serum at 37°C

Sara Goltry, Natalya Hallstrom, Tyler Clark, Wan Kuang, Jeunghoon Lee, Cheryl Jorcyk, William B. Knowlton, Bernard Yurke, William L. Hughes and Elton Graugnard, DNA topology influences molecular machine lifetime in human serum, Nanoscale, 2015, 7, 10382

(a–e) Representative native 10% PAGE gel sections for the unlabeled nanomachine and linear probe after incubation in 70% human serum at 37 °C. Incubation times are indicated above each lane and were the same for the nanomachine states and the Dark linear probe. The incubation times for the Bright linear probe were shorter due to its considerably shorter lifetime. The nanomachine and Dark linear probe have bands visible even after 48 hours of incubation in human serum, while the Bright linear probe is completely degraded within 6 hours. For this figure, image contrast has been enhanced uniformly for individual gels to enhance the visibility of the faint bands. (f) Mean lifetimes (mean ± SE) from the DNA nanomachine and linear probe incubated in 70% human serum at 37 °C. Lifetimes were estimated based on normalized band intensities of native PAGE experiments, as described in ESI S4.† These data indicate considerable differences in degradation rates. No data is shown for the Cy5.5-IBRQ Dark linear probe (red asterisk) due to purification issues associated with Cy5.5-IBRQ interaction (see ESI S3†).

DNA Devices in Various Solutions

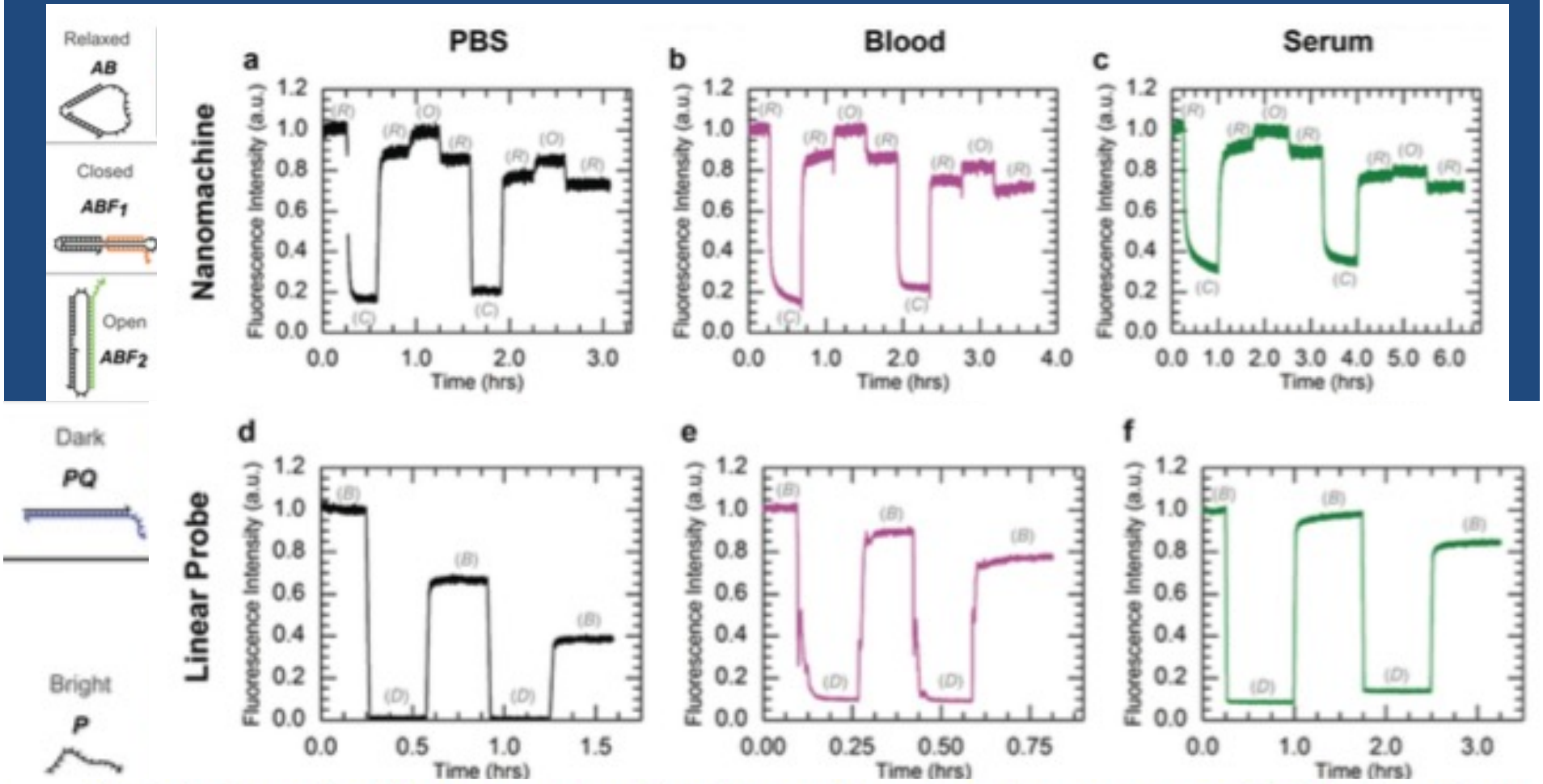

Kinetics data for operation of the three-state nanomachine and two-state linear probe. Both systems were operated in PBS (a, d), heparinized whole human blood (b, e), and human serum (c, f) through two complete cycles at 25 °C. The fluorescence data were normalized to the initial state intensities. The mechanical states of the nanomachine are Relaxed (R), Closed (C), and Open (O). The mechanical states of the linear probe are Bright (B) and Dark (D). Nanomachine data (a–c) include ~10% fluorescence offsets from excess A in solution. Aside from the Cy5.5-IBRQ interaction in the linear probe in PBS (d, see main text), the observed overall decreases in fluorescence for the Relaxed state of the nanomachine and the Bright state of the linear probe are attributed to dilutions from fuel injections. Stable operation was observed for both systems in all three solutions.

Operation of DNA Devices at 37°C

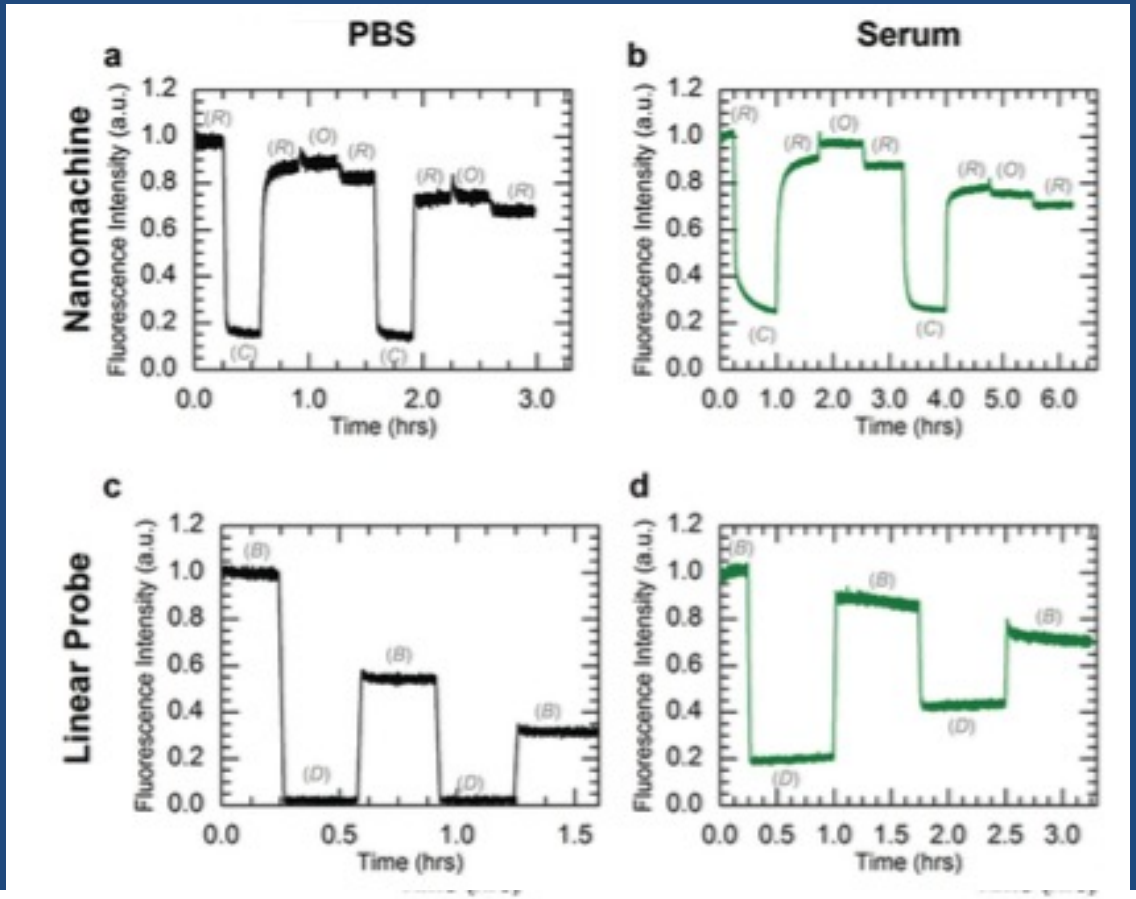

Kinetics data for operation of the three-state nanomachine and two-state linear probe at 37 °C. Both systems were operated in PBS (a, c) and human serum (b, d) through two complete cycles. The fluorescence data were normalized to the initial state intensities. The mechanical states of the nanomachine are Relaxed (R), Closed (C), and Open (O). The mechanical states of the linear probe are Bright (B) and Dark (D). Nanomachine data (a, b) include ~10% fluorescence offsets from excess *A* in solution. The observed overall decreases in fluorescence for the Relaxed state of the nanomachine and the Bright state of the linear probe are attributed to dilutions from fuel injections. (a) Operation of the nanomachine in PBS shows state transitions similar to 25 °C, but with unstable fluorescence in the Open state. (b) In serum, clear state transitions were observed for the first complete cycle, yet the Open state transition failed during the second cycle. Operation was arbitrarily terminated after two complete cycles. (c) Operation of the linear probe in PBS is consistent with results seen at 25 °C. (d) In human serum, the linear probe displayed a continuous increase in Dark state fluorescence, which is attributed to enzymatic degradation.

Absorption Spectrum for Whole Human Blood

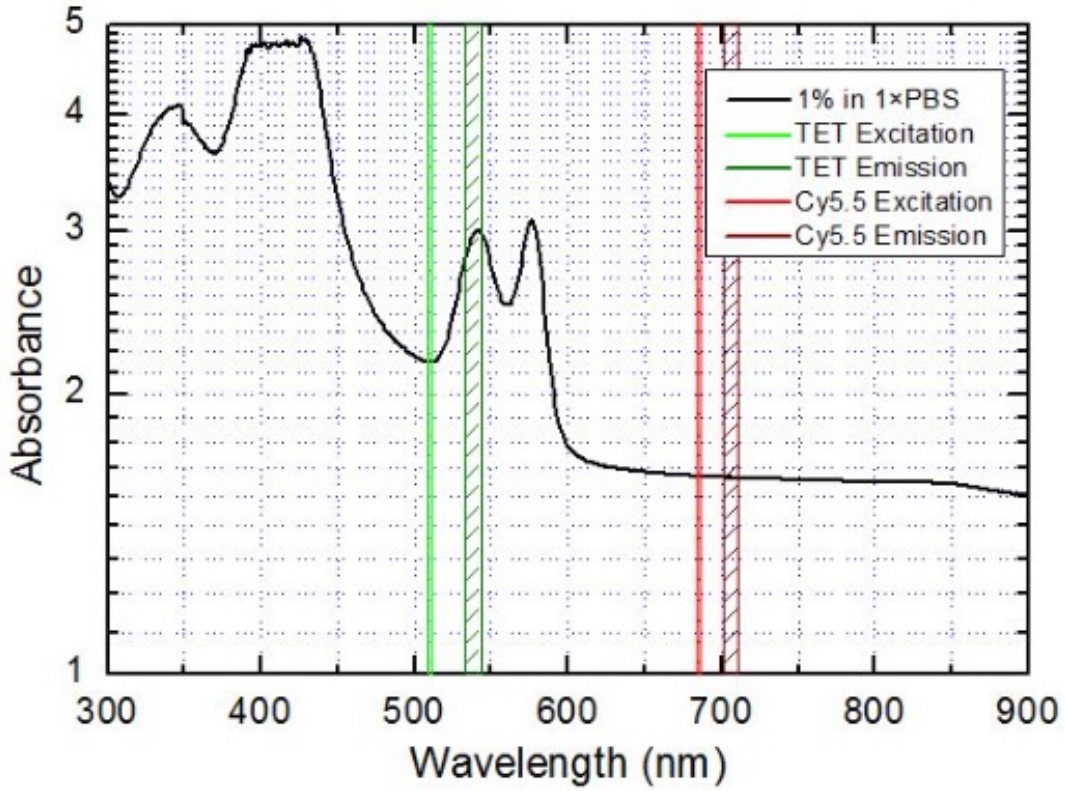

Absorption spectrum for a 1% solution of whole human blood in 1×PBS. For reference, the excitation and emission wavelengths and bandwidths for the TET and Cy5.5 dyes are indicated by the vertical hatched regions.

DNA Terminal Modifications for Protection in Serum

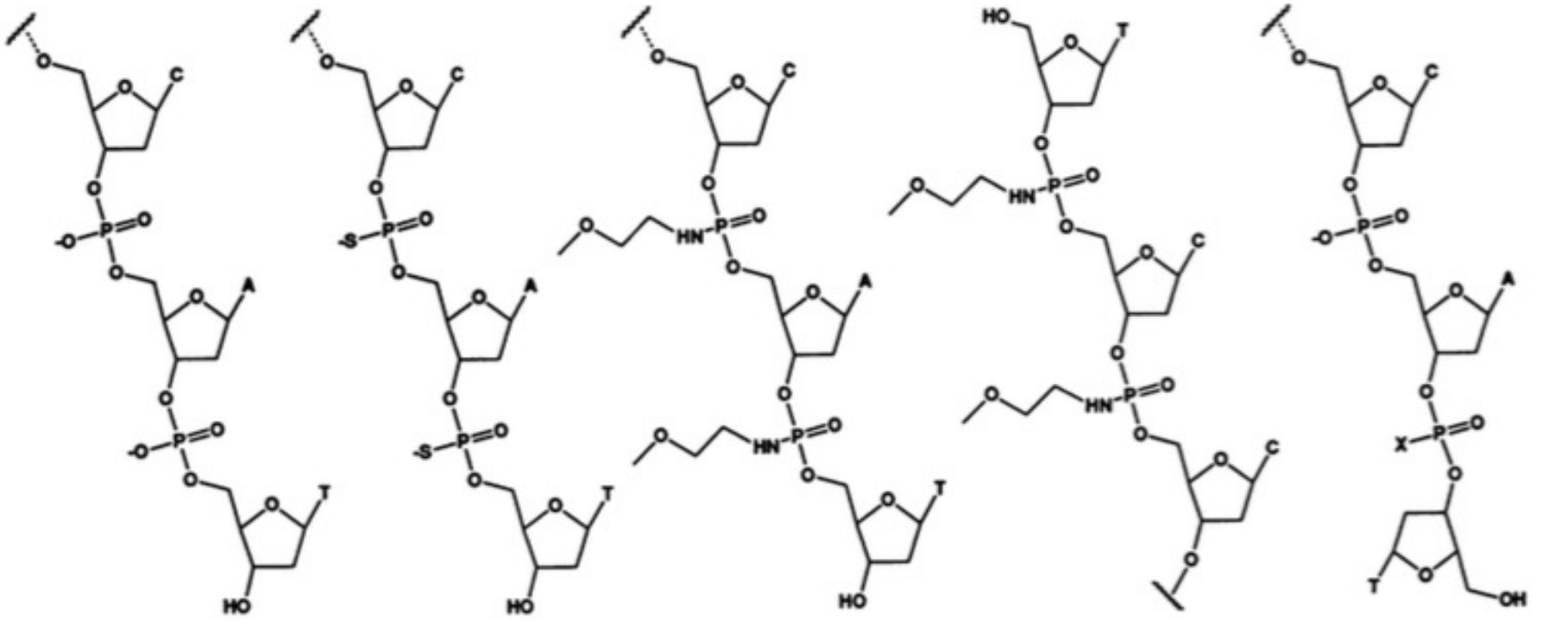

Jeng-Pyng Shaw, Kenneth Kent, Jeff Bird, James Fishback and Brian Froehler , Modified deoxyoligonucleotides stable to exonuclease degradation in serum, Nucleic Acids Research, Vol. 19, No. 4 747, 1991

Oligonucleotide Stability Analyses

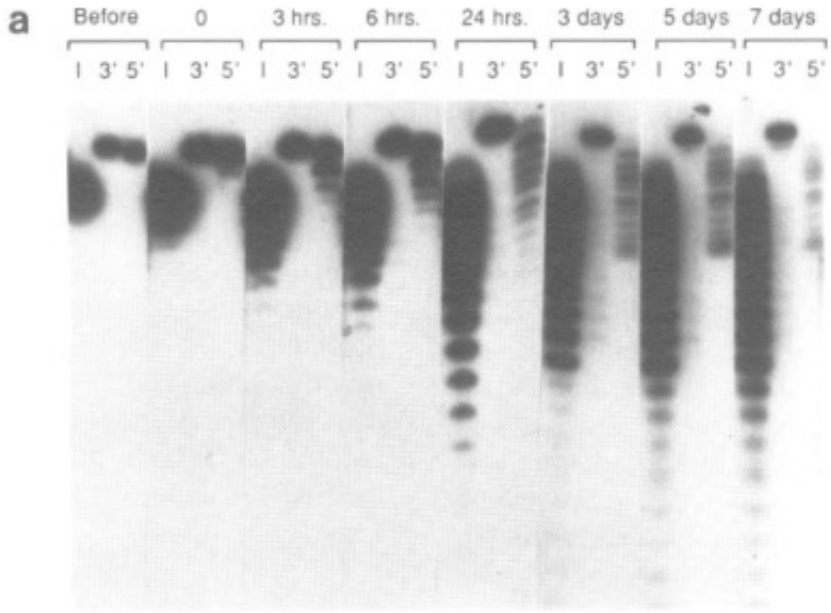

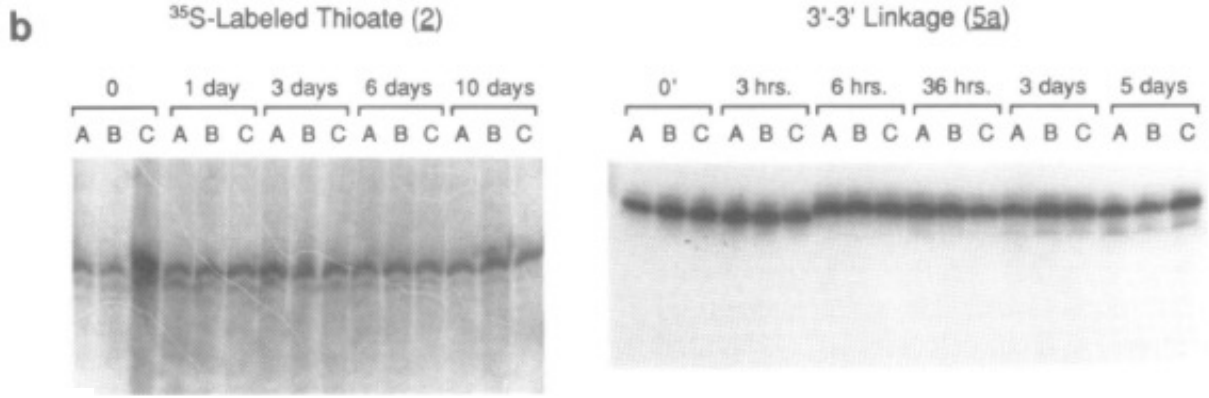

Jeng-Pyng Shaw, Kenneth Kent, Jeff Bird, James Fishback and Brian Froehler , Modified deoxyoligonucleotides stable to exonuclease degradation in serum, Nucleic Acids Research, Vol. 19, No. 4 747, 1991

Oligonucleotide stability study; internally labeled oligonucleotide was added to H938 cell culture at a final concentration of 20 μM. The oligonucleotides were recovered from the cell media at variable time-points and analyzed on 20% PAGE/7 *M* urea. 2a) I = internally labelled phosphodiester (*1*); 3′ = 3′-end cap (*3*); 5′ = 5′-end cap (*4*). 2b) ^{35}S labelled phosphorothioate (*2*); 3′-3′ inverted linkage (*5a*); A, B, and C represent triplicate sets of experiments.

Oligonucleotide Degradation in Serum

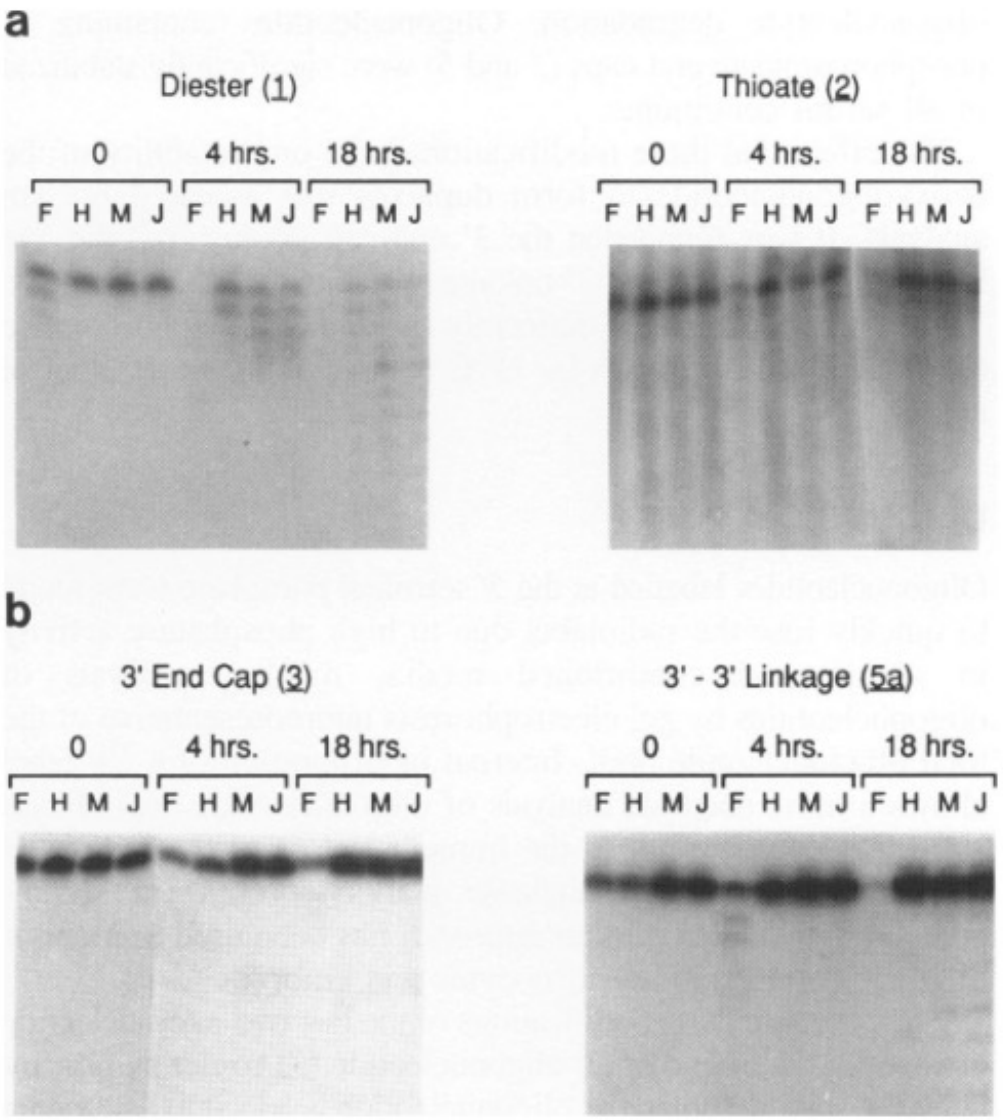

Oligonucleotide stability study in serum; internally labelled oligonucleotides were added to media containing 10% serum at a concentration of 10 n*M* and incubated at 37°C for 0, 4 or 18 hrs. Oligonucleotides were recovered and analyzed on 20% PAGE/7 *M* urea. F = fetal calf serum; H = heat inactivated fetal calf serum; M = sample 1 adult human serum; J = sample 2 adult human serum. 3a) Internally labeled phosphodiester (*1*) and ^{35}S labelled phosphorothioate (*2*). 3b) 3′-end cap (*3*) and 3′-3′ inverted linkage (*5a*).

Jeng-Pyng Shaw, Kenneth Kent, Jeff Bird, James Fishback and Brian Froehler , Modified deoxyoligonucleotides stable to exonuclease degradation in serum, Nucleic Acids Research, Vol. 19, No. 4 747, 1991

Table 1.

Oligonucleotide Analogue	Serum Half−Life FCS	Δ FCS	Cell Sup	T_m (°C)
Diester (*1*)	< 5 min	~ 4 hr	~ 3 hr	61.5
Thioate (*2*)	~ 4 hr	>> 18 hr	> 7 days	50.5
3′-EC (1 amidate) (*3*)	nd	nd	> 5 days	nd
3′-EC (2 amidate) (*3*)	~ 4 hr	>> 18 hr	> 7 days	61.0
5′-EC (2 amidate) (*4*)	< 5 min	~ 4 hr	~ 3 hr	nd
3′-3′ (diester) (*5a*)	~4 hr	>> 18 hr	> 7 days	61.0
3′-3′ (amidate) (*5b*)	~4 hr	>> 18 hr	> 7 days	nd

FCS: fetal calf serum; Δ FCS: heat inactivated fetal calf serum; Cell Sup: cellular supernatant; concentration of the oligonucleotide was 10 n*M*, nd−not determined.

Oligonucleotide Degradation in Serum

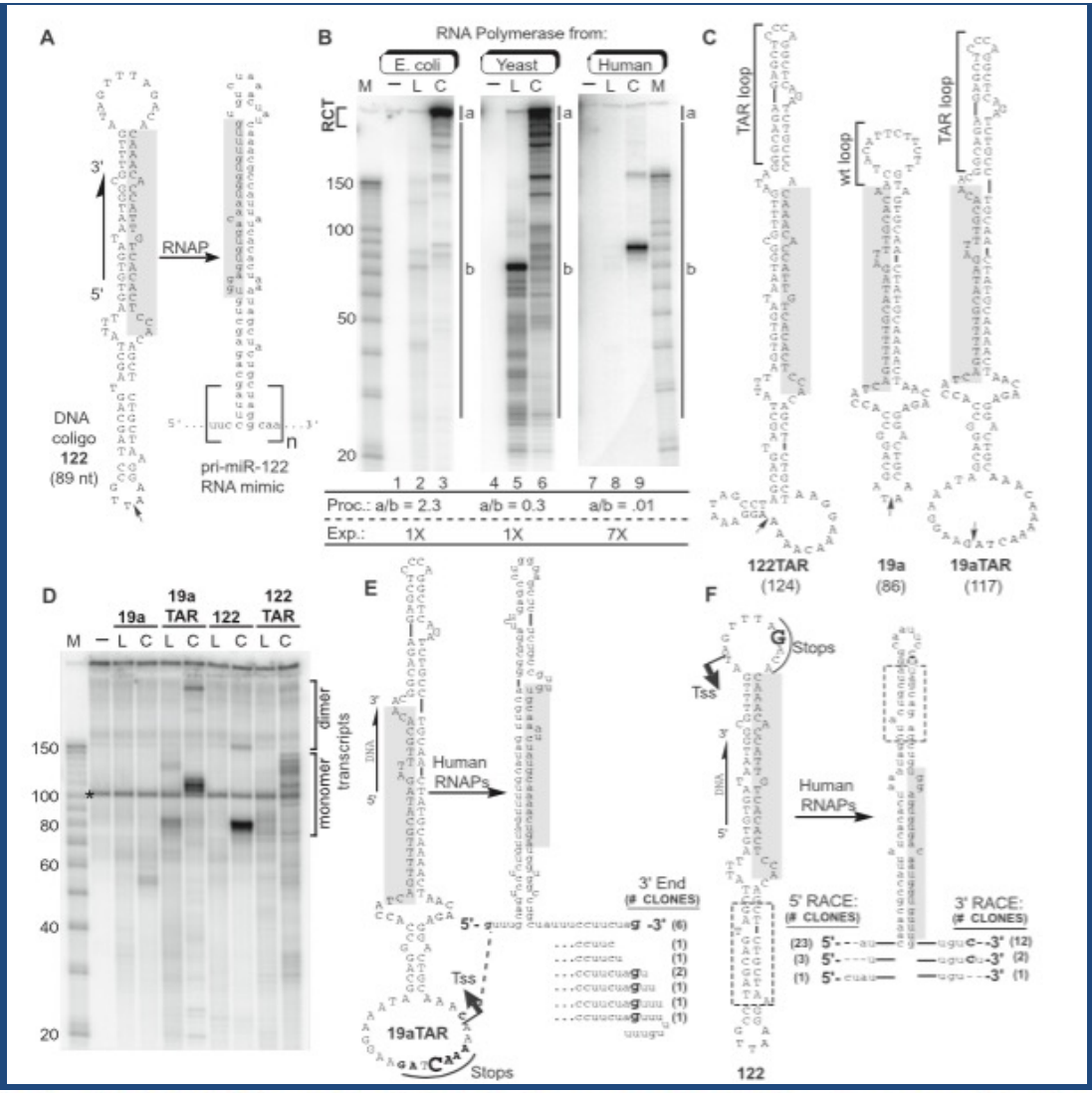

Transcription of coligos by RNAPs. (**A**) Schematic illustration showing the sequence and predicted secondary structure of a coligo and its RNA. Coligo **122** was taken from the template strand of the human gene encoding miR-122. The subscript **n** denotes number of tandem repeats. RCT produces **n** » 1; **n**~1 indicates single round transcription leading to monomer transcripts. Small arrow: circularization site, linear forms are discontinuous here with 5′ phosphate. Shaded region, mature miR-122 or its cDNA. nt, size in nucleotides. (**B**) IVT of coligo **122** by RNAPs of varying evolutionary age and complexity. *E. coli* RNAP, yeast RNAP II and human RNAPs from HEK293T WCE were used for IVT. RNA was visualized on a denaturing polyacrylamide gel (DPAGE) by uniform [α-^{32}P]-UTP incorporation. L, linear; C, coligo. Lanes 1, 4, 7: no template. M, RNA marker. Relative processivity (Proc.) defined by the a/b ratio, and relative exposure (Exp., i.e. Phosphorimager grayscale setting difference) are indicated. (**C**) Sequences and predicted secondary structures of coligos **122TAR**, **19a** and **19aTAR**. (**D**) IVT using HEK293T WCE followed by DPAGE analysis of uniformly labeled transcripts. Dimer transcripts read through the termination site one time to produce tandem dimer transcripts. (**E**) Sequence analysis of transcripts made by human WCE from coligo template **19aTAR**. The **19aTAR** IVT products were isolated and their cDNA sequenced. Tss, transcription start site. (**F**) Sequence analysis of transcripts made by human WCE from coligo template **122**. The **122** IVT product was isolated and sequenced using 5′ and 3′ RLM-RACE protocols.

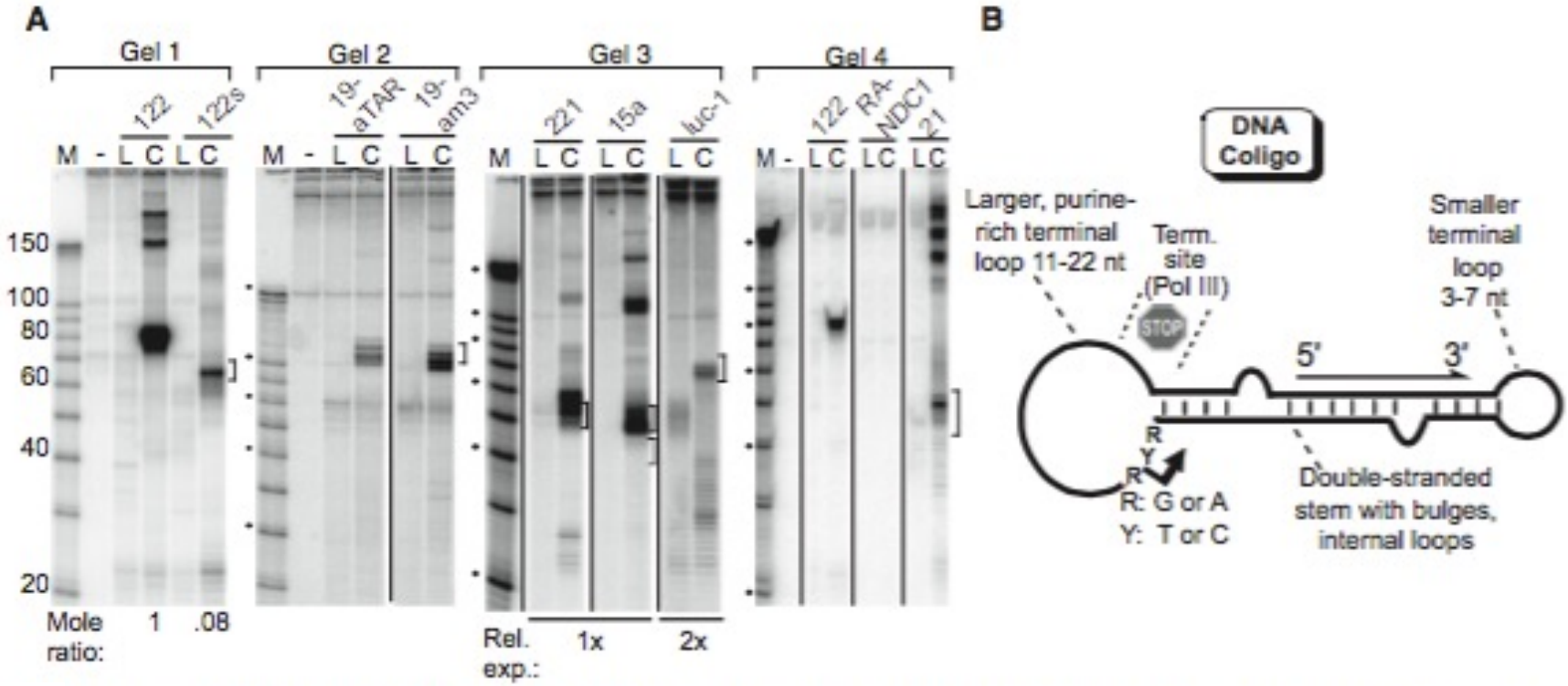

Coligo secondary structure contributes to transcription by human WCE. (**A**) IVT of indicated coligos, as in Figure 1. Coligo sequences and predicted secondary structures are shown in Supplementary Figure S2. Brackets indicate predicted monomer transcript size (10 nt window) based on sequencing data shown in Figure 1E and F. Gel 1: The boxed sequence shown in Figure 1F was removed from coligo **122** to produce **122s**, whose transcript size changed accordingly. Ratio is for monomer transcripts at 83 and 65 nt, adjusted for label content. Gel 2: The TAR loop encoding sequence in coligo **19aTAR** was changed while keeping a similar secondary structure to produce coligo **19am3**, which was similarly transcribed. Gel 3: Coligos **221** and **15a** are based on the human miRNAs of the same number. **Luc-1** encodes a pre-miRNA complementary to a luciferase 3′ UTR sequence. Each coligo was transcribed by WCE to predicted monomer-size transcripts (brackets). Gel 4: **RANDC1** encodes a largely unstructured transcript. Coligo **21** is based on human miR-21 and contains no RNAP III termination sites. It produces less monomer transcript and more tandem multimer transcripts. (**B**) Schematic summary of sequence and secondary coligo features that appear to promote discrete transcription events in WCE.

Oligonucleotide Degradation in Serum

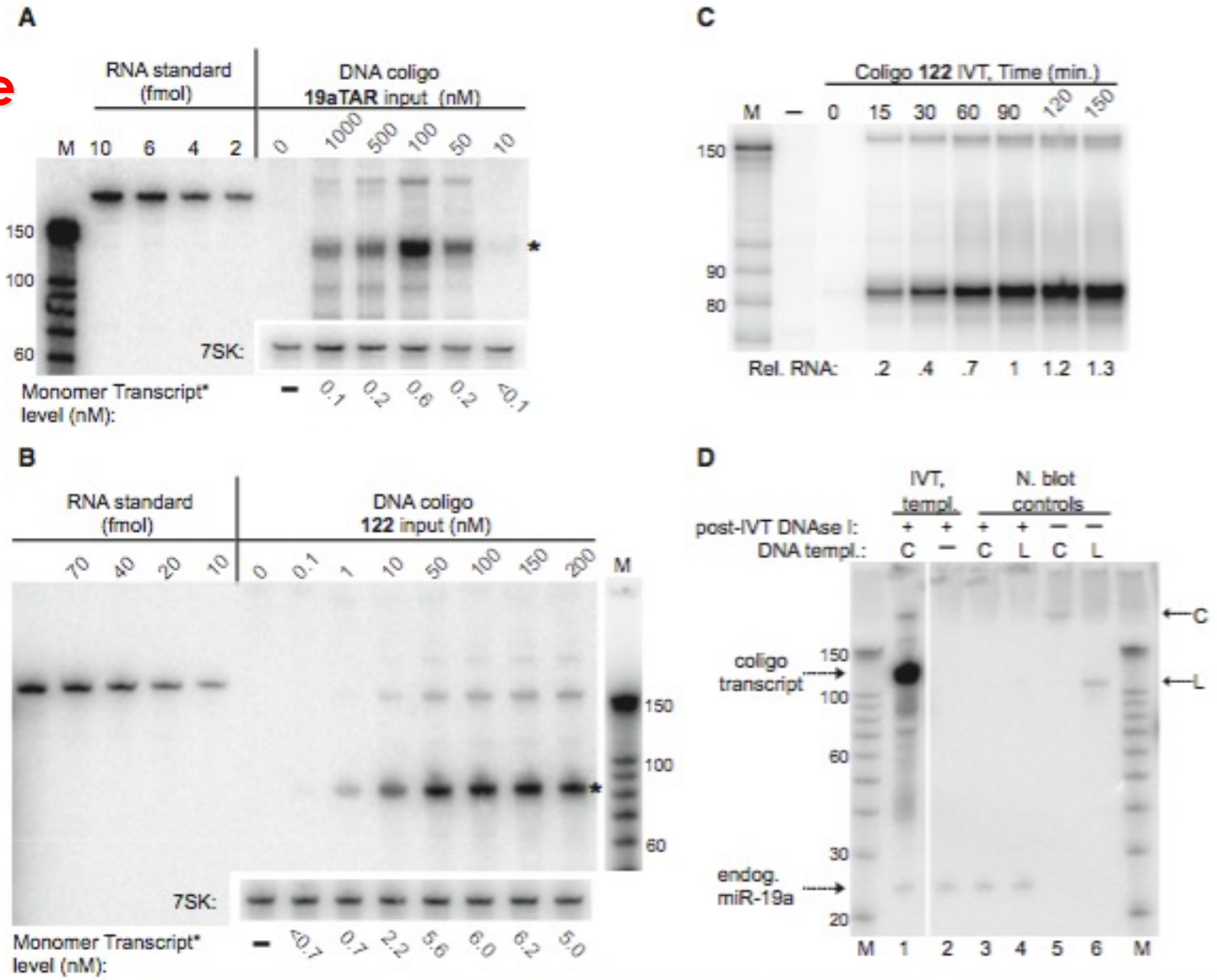

Coligo concentration dependence and RNA transcript quantitation for HEK293T WCE IVT. (**A**) Quantitative northern blotting of coligo **19aTAR** IVT transcripts. The indicated range of coligo concentrations was used in unlabeled HEK293T WCE IVT reactions and the transcript levels were compared with known amounts of RNA containing the same northern probe recognition sequence. Numbers below blot indicate transcript molarity estimated after 90 min IVT. Endogenous 7SK RNA was probed separately as a loading control. Asterisk (*) indicates the single round transcript whose concentration estimates are listed below gels. (**B**) Quantitative northern blotting of coligo **122** IVT transcripts, as in panel A. (**C**) Time course for 100 nM coligo **122** IVT, visualized by [α-^{32}P]-UTP incorporation. Rel. RNA: relative amount of RNA. (**D**) Quantitative LNA northern blot comparison of endogenous HEK293T miR-19a with the 90 min IVT transcripts made from coligo **19aTAR** (100 nM), in the same extract. The ratio of the **19aTAR** *in vitro* single-round transcript (~110 nt) to endogenous miR-19a (23 nt) is ~65. Full LNA northern signal cross-reacting with the DNA input templates, in absence of DNase treatment, can be seen in lanes 5 and 6. In lanes 3 and 4, the DNA templates were added to HEK293T extract and immediately processed without IVT incubation period to show that DNase I treatment of templates ensures they have no detectable signal in the northern blots shown in panels (A–C).

Oligonucleotide Degradation in Serum

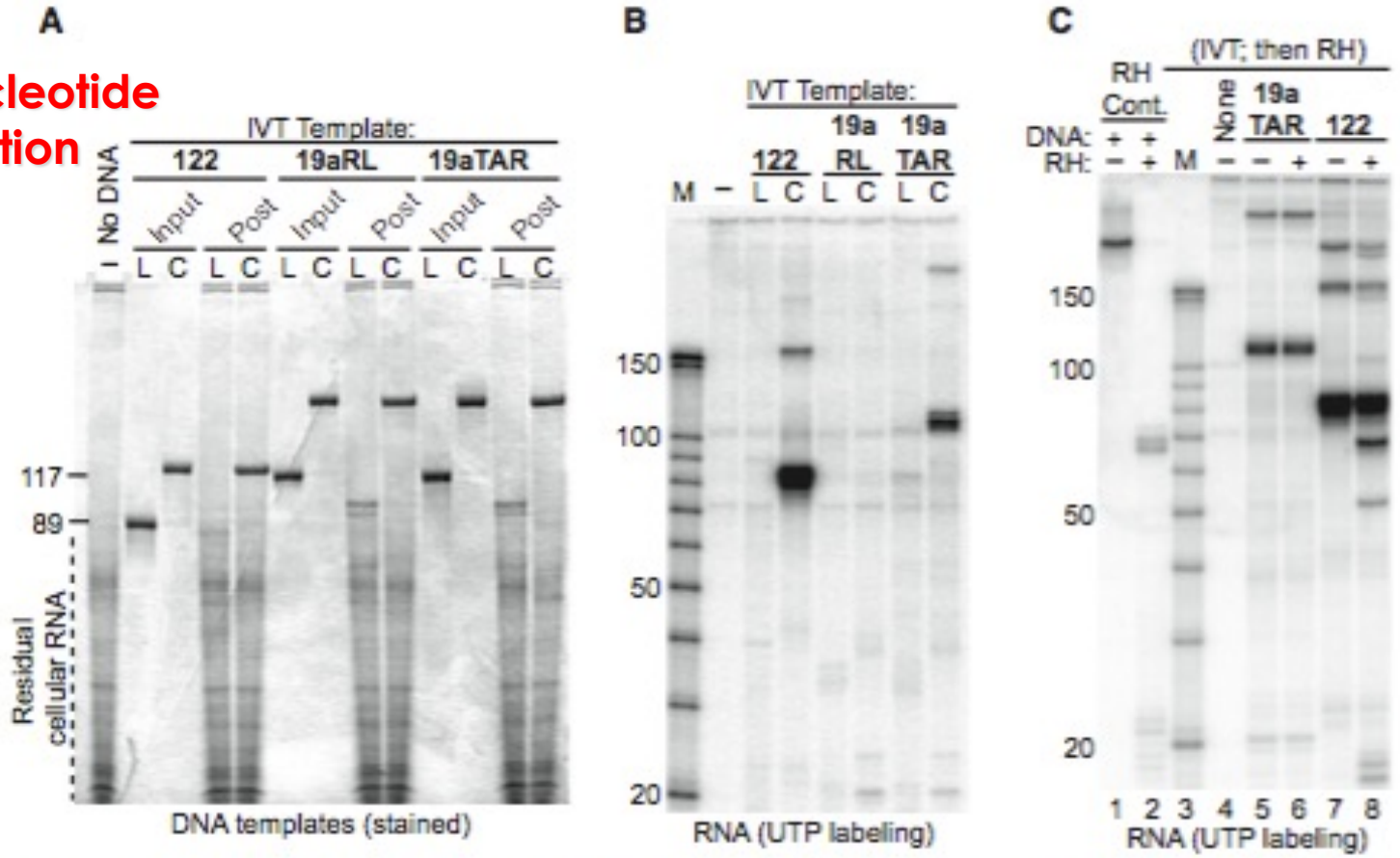

Coligo topology is necessary but not sufficient to template the synthesis of stable released sRNA transcripts in human WCE. (**A**) Circularization stabilizes oligonucleotides in human WCE. Circular (C) or linear (L) templates (Input) were recovered (Post) from HEK293T WCE IVT, digested with RNase cocktail to reduce cellular RNA, and stained after DPAGE. Linear forms were degraded during IVT; coligos were stable. Coligo **19aRL** sequence is shown in Supplementary Figure S2. (**B**) DPAGE separation of HEK293T WCE IVT of the three coligos and linear precursors from the reactions shown in panel A. (**C**) Transcripts are released from the coligo template during IVT. RNase H (RH) was added to (+) or withheld from (–) the indicated coligo IVT reactions at the end of a typical 90-min incubation period. Following additional incubation, the RNA products were separated by DPAGE. Lanes 1 and 2, validation of exhaustive RNase H activity on a ^{32}P-RNA:DNA hybrid. Reaction in lane 2 was supplemented with total HEK293T cellular RNA to normalize non-specific competing RNAs among all RNase H reactions. The result shows that the coligo **19aTAR**'s transcripts do not remain hybridized to the coligo template, while ~20% of coligo **122**'s transcripts do remain bound to the coligo template.

Oligonucleotide Degradation in Serum

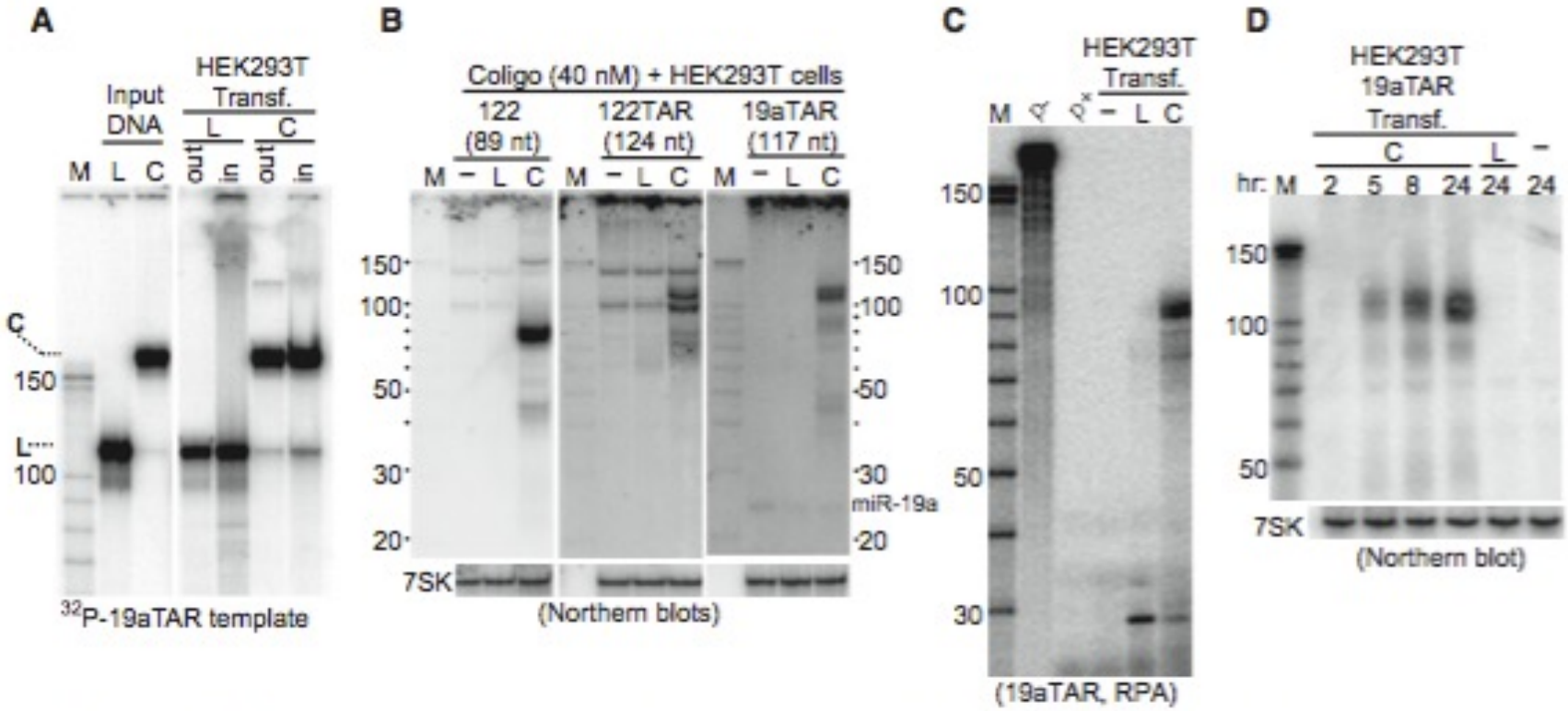

Coligo transcription in human cells. (**A**) Fate of transfected coligo and linear templates. ^{32}P-labeled DNA tracers were spiked into unlabeled templates and transfected at 40 nM into HEK293T cells using PolyFect transfection reagent. Templates recovered from harvested cells ('in') and media supernatant ('out') were adjusted to equal percentages of total fractions, and separated by DPAGE. C, coligo; L, linear; M, RNA marker. About half of the DNA entered cells during transfection. (**B**) Coligos are transcribed in human cells. Templates (C or L) were transfected into HEK293T cells for 24 h after which time total RNA was assayed by northern blotting using a 5′ labeled template-specific LNA. The ratio of the **19aTAR** single round transcript (~110 nt) to endogenous miR-19a (23 nt) is ~26. Endogenous 7SK RNA was probed separately as a loading control. (**C**) RPA on total RNA isolated from cells transfected with coligo or linear **19aTAR**. p–, probe input; p+, probe alone digested with RNase cocktail. (**D**) Coligo transcripts accumulate during transfection period. Total RNA of cells transfected with coligo **19aTAR** harvested after the indicated transfection times and probed by northern blotting using a uniformly labeled *in vitro* RNA transcript complementary to one complete coligo transcript sequence. 7SK, loading control.

Oligonucleotide Degradation in Serum

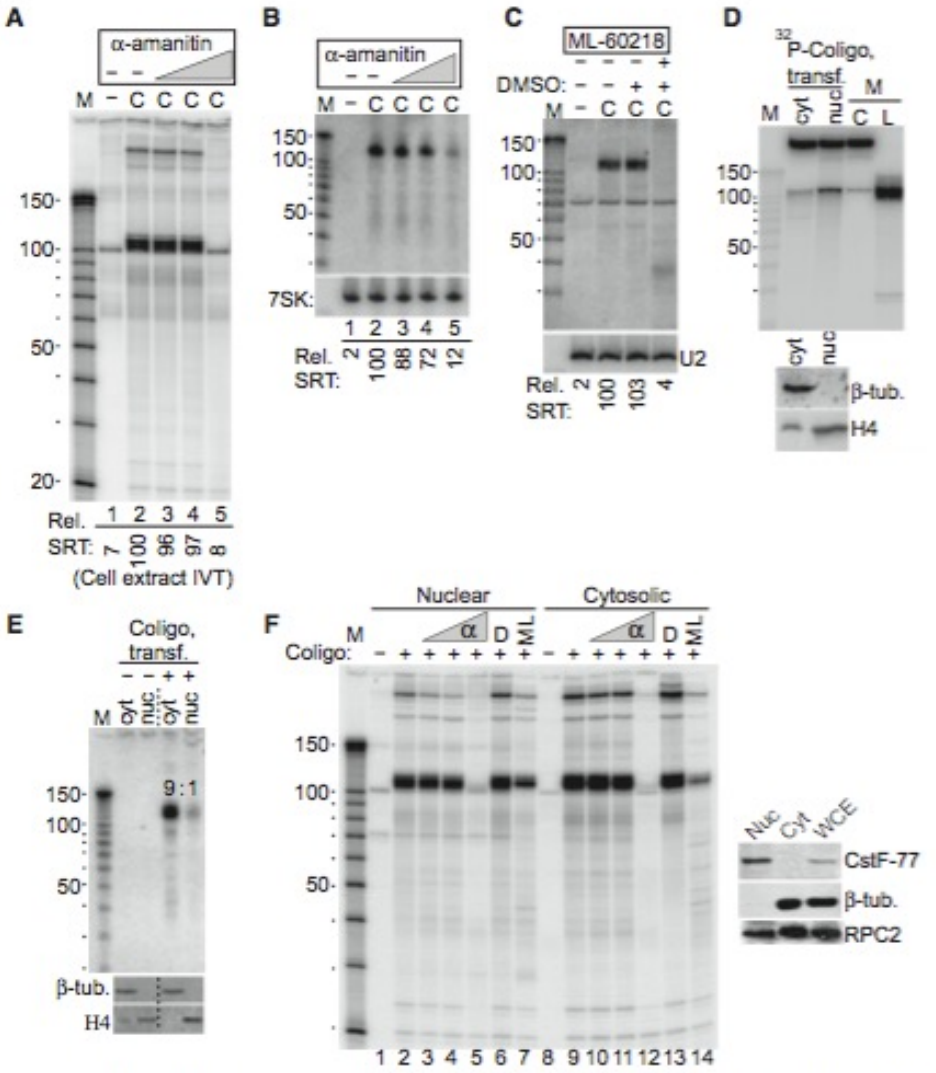

tNAP III is responsible for coligo transcription, which appears to take place mainly in the cytosol of transfected cells. (**A**) α-Amanitin inhibits coligo transcription at concentrations consistent with RNAP III transcription. HEK293T WCE IVT was carried out with increasing concentrations of α-amanitin. C, coligo **19aTAR**, 100 nM. Lanes 3–5: 0.12, 1.2, 120 μg/ml α-amanitin. Rel. SRT: relative amount of single round transcript (aka monomer transcript). (**B**) Northern blot of total RNA from HEK293T cells transfected with 40 nM coligo **19aTAR** with concurrent α-amanitin treatment (Lanes 3–5: 0.12, 1.2, 40 μg/ml). 7SK RNA was probed as a loading control. (**C**) Northern blot of total RNA from HEK293T cells transfected with 40 nM coligo **19aTAR** with concurrent RNAP III-specific inhibitor ML-60218 treatment at 68 μM. DMSO, inhibitor solvent. U2 snRNA was probed as loading control. (**D**) DPAGE of ^{32}P tracer-labeled coligo **19aTAR** recovered from HEK293T transfection after separation of nuclear and cytosolic fractions. Equal percentages of the nuclear and cytosolic fractions were loaded. Inset: western blot assessment of fractionation, β-tub., β-tubulin (cytosolic protein). H4, histone H4 (nuclear protein). M, markers and input templates. (**E**) Northern blot of RNA isolated from HEK293T nuclear and cytosolic fractions 24 h after transfection with 40 nM coligo **19aTAR**. Equal percentages of the nuclear and cytosolic fractions were loaded. Inset: western blot assessment of fractionation, as in panel D. (**F**) HEK293T nuclear and cytosolic extract IVT in the presence of increasing α-amanitin (α, lanes 3–5 and 10–12: 0.12, 1.2 and 120 μg/ml), DMSO (D) or ML-60218/DMSO solution (ML). Inset: western blot assessment of fractionation, β-tub., β-tubulin (cytosolic protein). CstF-77, (nuclear protein); RPC2, RNAP III subunit.

Further References

- S. Goltry *et al.*, DNA topology influences molecular machine lifetime in human serum. ***Nanoscale* 7**, 10382-10390 (2015)
- J. P. Shaw, K. Kent, J. Bird, J. Fishback, B. Froehler, Modified deoxyoligonucleotides stable to exonuclease degradation in serum. ***Nucleic acids research* 19**, 747-750 (1991).
- B. C. Chu, L. E. Orgel, The stability of different forms of double-stranded decoy DNA in serum and nuclear extracts. ***Nucleic acids research* 20**, 5857-5858 (1992).
- I. M. Khan, J. M. Coulson, A novel method to stabilise antisense oligonucleotides against exonuclease degradation. ***Nucleic acids research* 21**, 4433 (1993).
- Y. J. Chen, B. Groves, R. A. Muscat, G. Seelig, DNA nanotechnology from the test tube to the cell. ***Nature nanotechnology* 10**, 748-760 (2015).
- C. I. Seidl, L. Lama, K. Ryan, Circularized synthetic oligodeoxynucleotides serve as promoterless RNA polymerase III templates for small RNA generation in human cells. ***Nucleic acids research* 41**, 2552-2564 (2013).